Published in final edited form as:
Science. 2022 June 10; 376(6598): eabm9798. doi:10.1126/science.abm9798.

Architecture of the linker-scaffold in the nuclear pore

Stefan Petrovic[1], **Dipanjan Samanta**[1,#], **Thibaud Perriches**[1,#,†], **Christopher J. Bley**[1], **Karsten Thierbach**[1,‡], **Bonnie Brown**[1], **Si Nie**[1], **George W. Mobbs**[1], **Taylor A. Stevens**[1], **Xiaoyu Liu**[1,§], **Giovani Pinton Tomaleri**[1], **Lucas Schaus**[1], **André Hoelz**[1,*]

[1]California Institute of Technology, Division of Chemistry and Chemical Engineering, 1200 East California Boulevard, Pasadena, CA 91125, USA

Abstract

Nuclear pore complexes (NPCs) mediate the nucleocytoplasmic transport of macromolecules. Although the arrangement of the structured scaffold nucleoporins in the NPC's symmetric core had been determined, their cohesion by multivalent unstructured linker nucleoporins remained elusive. Combining biochemical reconstitution, high-resolution structure determination, docking into cryo-electron tomographic reconstructions, and physiological validation, we elucidated the architecture of the evolutionarily conserved linker-scaffold, yielding a near-atomic composite structure of the human NPC's ~64MDa symmetric core. Whereas linkers generally play a rigidifying role, the linker-scaffold of the NPC provides the plasticity and robustness necessary for the reversible constriction and dilation of its central transport channel and the emergence of lateral channels. Our results substantially advance the structural characterization of the NPC symmetric core, providing a basis for future functional studies.

INTRODUCTION—In eukaryotic cells, the selective bidirectional transport of macromolecules between the nucleus and cytoplasm occurs through the nuclear pore complex (NPC). Embedded in nuclear envelope pores, the ~110MDa human NPC is an ~1,200Å wide and ~750Å tall assembly of ~1,000 proteins, collectively termed nucleoporins. Because of the NPC's eight-fold rotational symmetry along the nucleocytoplasmic axis, each of the ~34 different nucleoporins occurs in multiples of eight. Architecturally, the NPC's symmetric core is composed of an inner ring encircling the central transport channel, and two outer rings anchored on both sides of the nuclear

---

[*] Corresponding author. hoelz@caltech.edu (A.H.).
[†] Present address: Care Partners, 146 chemin de l'Etang, 69380 Dommartin, France.
[‡] Present address: Odyssey Therapeutics, Inc., Industriepark Höchst, G875, 65926 Frankfurt am Main, Germany.
[§] Present address: Department of Microbiology, Immunology & Molecular Genetics, University of California, Los Angeles, 609 Charles E. Young Drive East, Los Angeles, CA 90095, USA.
[#] These authors contributed momentously and equally to this work.

Author contributions: AH conceived and coordinated the study. SP, DS, TP, CJB, KT and AH designed research. SP, DS, TP, CJB, KT, BB, GPT, and LS performed research. SP, DS, TP, CJB, KT, BB, SN, GWM, TAS, XL, GPT, LS, and AH analyzed data. SP, DS, TP, CJB, and AH integrated and conceptualized the results. SP, CJB, SN, GWM, and AH wrote and revised the manuscript, with contributions from all authors.

Competing interests: The authors declare no financial conflicts of interest.

Supplementary Materials:
Materials and Methods
Supplementary Text
Figs. S1 to S83
Tables S1 to S16
References (90–148)
Movies 1 to 5

envelope. Because of its central role in the flow of genetic information from DNA to RNA to protein, the NPC is commonly targeted in viral infections and its nucleoporin constituents are associated with a plethora of diseases.

RATIONALE—Although the arrangement of most scaffold nucleoporins in the NPC's symmetric core was determined by quantitative docking of crystal structures into cryo-electron tomographic (cryo-ET) maps of intact NPCs, the topology and molecular details of their cohesion by multivalent linker nucleoporins have remained elusive. Recently, *in situ* cryo-ET reconstructions of NPCs from various species have indicated that the NPC's inner ring is capable of reversible constriction and dilation in response to variations in nuclear envelope membrane tension, thereby modulating the diameter of the central transport channel by ~200Å. We combined biochemical reconstitution, high resolution crystal and single particle cryo-electron microscopy (cryo-EM) structure determination, docking into cryo-ET maps, and physiological validation to elucidate the molecular architecture of the linker-scaffold interaction network that is not only essential for the NPC's integrity, but also confers the plasticity and robustness necessary to allow and withstand such large-scale conformational changes.

RESULTS—By biochemically mapping scaffold-binding regions of all fungal and human linker nucleoporins and determining crystal and single particle cryo-EM structures of linker-scaffold complexes, we completed the characterization of the biochemically tractable linker-scaffold network and established its evolutionary conservation, despite considerable sequence divergence. We determined a series of crystal and single particle cryo-EM structures of the intact Nup188 and Nup192 scaffold hubs bound to their Nic96, Nup145N, and Nup53 linker nucleoporin binding regions, revealing that both proteins form distinct question mark-shaped keystones of two evolutionarily conserved hetero-octameric inner ring complexes. Linkers bind to scaffold surface pockets via short defined motifs, with flanking regions commonly forming additional disperse interactions that reinforce the binding. Employing a structure-guided functional analysis in *S. cerevisiae*, we confirmed the robustness of linker-scaffold interactions and established the physiological relevance of our biochemical and structural findings. The near-atomic composite structures resulting from quantitative docking of experimental structures into human and *S. cerevisiae* cryo-ET maps of constricted and dilated NPCs structurally disambiguated the positioning of the Nup188 and Nup192 hubs in the intact fungal and human NPC and revealed the topology of the linker-scaffold network. The linker-scaffold gives rise to eight relatively rigid inner ring spokes, flexibly inter-connected to allow for the formation of lateral channels. Unexpectedly, we uncovered that linker-scaffold interactions play an opposing role in the outer rings by forming tight cross-link staples between the eight nuclear and cytoplasmic outer ring spokes, thereby limiting the dilatory movements to the inner ring.

CONCLUSIONS—We have substantially advanced the structural and biochemical characterization of the symmetric core of the *S. cerevisiae* and human NPCs and determined near-atomic composite structures. The composite structures uncover the molecular mechanism by which the evolutionarily conserved linker-scaffold establishes the NPC's integrity, while simultaneously allowing for the observed plasticity of the central transport channel. The composite structures are roadmaps for the mechanistic dissection of NPC assembly and disassembly, the etiology of NPC-associated diseases, the role of NPC dilation in nucleocytoplasmic transport of soluble and integral membrane protein cargoes, and the anchoring of asymmetric nucleoporins.

One-Sentence Summary:

An interdisciplinary analysis established the near-atomic molecular architecture and evolutionary conservation of the linker-scaffold of the human nuclear pore complex.

The enclosure of genetic material in the nucleus requires the selective transport of folded proteins and ribonucleic acids across the nuclear envelope, for which the nuclear pore complex (NPC) is the sole gateway (1–4). Beyond its function as a selective, bidirectional channel for macromolecules, the role of the NPC extends to genome organization, transcription regulation, mRNA maturation, and ribosome assembly (1, 2). The NPC and its components are implicated in the etiology of many human diseases, including viral infections (5, 6). The building blocks of the NPC are a set of ~34 different proteins collectively termed nucleoporins (nups). In the NPC, nups assemble into defined subcomplexes that are generally present in multiples of eight, adding up to a mass of ~110MDa in the human NPC (1–4). The NPC architecture consists of a symmetric core with asymmetric decorations on its nuclear and cytoplasmic faces (Fig.1A). The symmetric core displays eight- and two-fold rotational symmetry about the nucleocytoplasmic axis and axes coplanar with the nuclear envelope, respectively. It consists of two outer rings that sit on top of the nuclear envelope and an inner ring that lines the lumen generated by the fusion of the two lipid bilayers of the nuclear envelope. From the inner ring, unstructured phenylalanine-glycine (FG) repeats are projected into the central transport channel to establish the diffusion barrier. Although ~40kDa has historically been considered the threshold for passive diffusion (7, 8), the size selectivity of the barrier shows a more gradual dependence on molecular mass (9). Active transport is generally mediated by karyopherins, whose affinity for FG repeats and ultrafast exchange kinetics allow karyopherin-bound cargo to traverse the diffusion barrier (10–13).

The structural characterization of the NPC has progressed through efforts to reconstitute and crystallize ever larger portions of it, from small nup domain fragments to complexes as large as the ~400kDa hetero-heptameric Y-shaped coat nup complex (CNC) (14–30). In parallel, progress has been driven by efforts to push the resolution of cryo-electron tomographic (cryo-ET) reconstructions of intact NPCs (31). The docking of the CNC crystal structure into an ~32Å cryo-ET map of the intact human NPC was the first demonstration that biochemical reconstitution and crystal structures could be used to interpret cryo-ET maps and unraveled the head-to-tail tandem arrangement of CNCs in the outer rings (29, 32). The reconstitution and piecemeal structural analysis of two hetero-nonameric ~425kDa inner ring complexes (IRCs) provided the basis for docking 17 symmetric core nups into an ~23Å cryo-ET map of the intact human NPC (28, 33), yielding a near-atomic composite structure of the entire ~56MDa symmetric core of the human NPC (34, 35). A similar approach elucidated the near-atomic architectures of constricted and dilated states of the *S.cerevisiae* NPC using crystal structures to interpret ~25Å cryo-ET maps (36, 37). Apart from an additional distal CNC ring and associated nups present in the outer rings of the human NPC, the human and *S.cerevisiae* NPC present equivalent nup arrangements (34–38).

The inner ring of the human NPC is composed of six scaffold nups NUP155, NUP188, NUP205, NUP54, NUP58, and NUP62, two primarily unstructured linker nups NUP53 and NUP98, and NUP93, which is a hybrid of both (34, 35). The doughnut-shaped inner ring adopts a concentric cylinder architecture, in which membrane-anchored NUP155 forms the outermost coat, followed by layers of NUP93, NUP205/NUP188, and the NUP54•NUP58•NUP62 channel nucleoporin hetero-trimer (CNT) in the center, providing the FG repeats to form the diffusion barrier in the central transport channel. Unlike the extensive interactions of large, folded domains found in the CNC (16–20, 22, 25, 27, 29, 39), the structured domains of the inner ring nups do not interact directly. Instead, the inner ring is held together by the linker nups NUP53, NUP98, and the linker region of NUP93, which are proposed to connect the scaffolds of the four layers (28, 33, 35, 40–42). The resulting linker-scaffold architecture allows for a substantial ~200Å dilation of the inner ring's central transport channel, accompanied by the generation of lateral channels between the eight spokes, as observed in recent cryo-ET analyses of purified and *in situ* human and fungal NPCs (36, 43–46). The linker-scaffold is expected to play a fundamental role in establishing an architectural framework to accommodate the structural changes associated with the reversible constriction and dilation of the inner ring.

Whereas our previous work achieved the identification of the majority of the scaffold nup locations in the NPC, a comprehensive understanding and the molecular details of the linker-scaffold interaction network that mediates the cohesion of the symmetric core has remained elusive. Here, we report the characterization of the complete tractable set of linker-scaffold interactions through residue-level biochemical mapping of scaffold-binding regions in linker nups and the determination of crystal and single particle cryo-EM structures of linker-scaffold complexes. Our analysis revealed a common linker-scaffold binding mode, whereby linkers are anchored by central structured motifs whose binding is reinforced by disperse interactions of flanking regions. We quantitatively docked the complete set of linker-scaffold structures into an ~12Å cryo-ET reconstruction of the human NPC (provided by Martin Beck's group) (47), and an ~25Å *in situ* cryo-ET reconstruction of the *S.cerevisiae* NPC (36). In the inner ring, our new linker-scaffold structures allowed for the unambiguous assignment of NUP188 and NUP205 to 16 peripheral and 16 equatorial positions, respectively. From the nuclear envelope to the central transport channel, linkers bridge the layers of the inner ring to coalesce scaffold nups into eight relatively rigid spokes that are flexibly inter-connected, allowing for the formation of lateral channels. The linker-scaffold confers the plasticity necessary for the reversible dilation and constriction of the inner ring in response to alterations in nuclear envelope membrane tension. The topology of linker-scaffold interactions between inner ring nups is conserved from fungi to humans. We carried out systematic functional analyses of the linker-scaffold network, including the development of a minimal linker *S.cerevisiae* strain, establishing its robustness and essential nature. Our quantitative docking analysis of the human NPC revealed eight NUP205•NUP93 complexes that cross-link adjacent spokes in both nuclear and cytoplasmic outer rings. Facing the central transport channel, additional eight NUP205•NUP93 copies are exclusively anchored at the base of the cytoplasmic outer ring. NUP93 emerges as a versatile linker-scaffold hybrid that recruits and positions the FG repeat-harboring CNT to the inner ring and reinforces the tandem head-to-tail CNC arrangement in the outer rings, explaining its fundamental role in maintaining the integrity of the entire NPC. Our analysis substantially advances the structural characterization of the ~64MDa symmetric core and lays out a roadmap for future studies on the NPC assembly and function.

RESULTS

Biochemical and structural analysis of *C.thermophilum* linker-scaffold interactions

Nup192 and Nup188 are question mark shaped scaffold keystones of two alternative eight-protein inner ring complexes, both of which include the linkers Nup145N, Nup53, and the scaffold-linker hybrid Nic96 (Fig.1, B to D) (28, 33, 35, 40, 41). Previously, a composite structure of the full-length ~200kDa Nup192 was determined by superposing overlapping structures of its N- and C-terminal parts, revealing an extended α-helical solenoid with a question mark-shaped architecture, composed of five HEAT and fifteen ARM repeats, and a prominent central Tower (35, 40, 41, 48). High-resolution structures of Nup188 encompassing the ~130kDa N-terminal domain (NTD), which contains a central SH3-like domain insertion, and the ~45kDa C-terminal Tail region again revealed extended α-helical solenoids composed of ARM and HEAT repeats (28, 49). However, no structural information could so far be obtained for the ~32kDa Nup188 central region equivalent to the Nup192 Tower. Although binding of Nup192 and Nup188 has been biochemically mapped to the Nic96, Nup53 and Nup145N linkers, the molecular details are unknown. To gather these details, crucial to the elucidation of the linker-scaffold architecture, we performed the following comprehensive biochemical and structural analyses.

Nup192 interaction with Nic96.—Utilizing a crystallizable Nup192$^{\Delta\text{Head}}$ (residues 153–1756) fragment (35), we obtained co-crystals with our previously biochemically mapped Nic96$^{187–301}$ fragment that diffracted to 3.6Å resolution (fig.S1). Nic96 residues 187–239 were not resolved and were found to be dispensable for Nup192 binding by isothermal titration calorimetry (ITC), as both Nic96$^{187–301}$ and Nic96^{R2} (residues 240–301) retained a dissociation constant (K_D) of ~75nM (Fig.2E, fig.S2, A and D). The Nic96^{R2} sequence register was unambiguously assigned by identifying seleno-L-methionine (SeMet)-labeled residues in anomalous difference Fourier maps (fig.S1). To obtain the structure of full-length Nup192•Nic96^{R2}, we determined a single particle cryo-EM reconstruction at 3.8Å global resolution from a refined set of 176,609 particles whose preferential orientation resulted in an anisotropic 3.5–4.0Å directional Fourier shell correlation (FSC) resolution range (Fig.2B, fig.S3). Nic96^{R2} forms two amphipathic α-helices connected via a sharply kinking loop that extend from the midpoint to the base of the Nup192 question mark-shaped α-helical solenoid. The longer N-terminal α-helix is cradled by the concave Nup192 surface formed by ten ARM and HEAT repeats and the central Tower, while the shorter C-terminal α-helix packs against a hydrophobic patch formed from the C-terminal Nup192 α-helices α75–77 (ARM-20). Comparison of our crystal and cryo-EM structures confirmed the molecular details of Nic96^{R2} binding and identified a conformational difference in the width of the gap between the Nup192 Head and Tower subdomains (fig.S4). To validate the molecular details of the Nup192-Nic96^{R2} interface, we performed structure-guided mutagenesis and assessed binding by size-exclusion chromatography coupled to multi-angle light scattering (SEC-MALS) and ITC. Consistent with an ~3,700Å^2 hydrophobic interface, binding was not strongly affected by individual substitutions, but only abolished by Nic96 FFF or Nup192 LAF combination mutations (Fig.2, C to F, figs.S2, S5 to S7).

Nup188 interaction with Nic96.—Next, we tested whether the same Nic96 region was sufficient for Nup188 binding. Indeed, ITC measurements revealed that Nup188 binds both Nic96^{R2} and Nic96$^{187–301}$ with similar K_D*s* of ~90nM (Fig.2J and fig.S8, A and D). We determined crystal structures of Nup188•Nic96^{R2} and Nup188^{NTD} (residues 1–1134) at 4.4Å and 2.8Å resolution, respectively, the latter of which aided with phasing and model-building. The Nup188 and Nic96^{R2} sequence registers were unambiguously assigned by identifying SeMet-labeled residues in anomalous difference Fourier maps (Fig.2G and fig.S9). Like Nup192, Nup188 adopts an overall question mark-shaped architecture, composed of an N-terminal Head subdomain, 9 HEAT, 13 ARM repeats, and a central, comparatively more compact Tower (Fig.2G). Similarly, Nic96^{R2} binds a concave surface between the midpoint and the base of the Nup188 question mark-shaped α-helical solenoid, burying ~3,700Å^2 of combined surface area. Although Nup188-bound Nic96^{R2} also forms two amphipathic α-helices, the α-helices start and end at different residues, resulting in a secondary structure that radically differs from the Nup192-bound form (Fig.2, B and G). Nup188-bound Nic96^{R2} has a shorter N-terminal helix that binds to the central Tower, and a longer C-terminal helix cradled in the concave surface at the base of Nup188 (Fig.2G). Remarkably, the Nic96^{R2} FFF mutation that abolishes Nup192 binding had the same effect on Nup188 binding, despite the structural polymorphism between Nup192- and Nup188-bound Nic96^{R2} (Fig.2, H to K, figs.S8B, S10, and S12). Analogous to the Nup192 LAF mutant, we identified a triple Nup188 FLV substitution that disrupted Nic96^{R2} binding (Fig.2, I to K, figs.S8C, S11, and S12).

Nup192 interaction with Nup145N and Nup53.—To identify the Nup145N regions necessary and sufficient for Nup192 binding, we performed a five-alanine scanning mutagenesis and truncation analysis of Nup145N (Fig.3A). Substituting five consecutive residues at a time to alanines, we found a hotspot between residues 626–655 that displayed diminished binding to Nup192 (Fig.3A and fig.S13). N- and C-terminal Nup145N truncation resulted in a minimal Nup145N^{R1} peptide (residues 616–683) that recapitulated the Nup192-Nup145N interaction, although shorter Nup145N fragments showed residual binding to Nup192 (Fig.3B and fig.S14). ITC measurements confirmed that Nup192 binding is primarily sustained by Nup145N’s R1 region, with K_Ds of ~825nM and ~1,600nM for Nup145N and Nup145N^{R1} binding, respectively (Fig.3G and fig.S15).

With our previously mapped minimal Nup53^{R1} fragment (residues 31–67) (41), we reconstituted an ~220kDa Nup192•Nic96^{R2}•Nup145N^{R1}•Nup53^{R1} complex and obtained a single particle cryo-EM reconstruction at 3.2Å global resolution from a selected set of 484,910 particles whose preferential orientation resulted in an anisotropic 3.1–3.6Å directional FSC resolution range (Fig.3C and fig.S16). For Nup53^{R1}, the cryo-EM map only resolved the central phenylalanine-glycine (FG) dipeptide buried in a hydrophobic pocket at the top of the Nup192 molecule. Key contacts involve L441 and W499 of Nup192 and F48 of Nup53, uniquely consistent with our previous identification of these residues as required for the Nup53^{R1}-Nup192 interaction by systematic mutagenesis (Fig.3D) (41).

The Nup145N^{R1} binding site is proximal to the Nic96^{R2} binding site, at the midpoint of the question mark-shaped Nup192, where a hydrophobic pocket anchors the Nup145N^{R1} MYKL motif (residues 633–636) that runs perpendicular to the long axis of the question mark, with its N-terminus oriented towards the N-terminus of Nic96^{R2} (Fig.3E). Overall, comparison of the Nup192 structures in complex with different linkers demonstrated that linker binding does not induce conformational rearrangements in the scaffold Nup192 (fig.S17).

Validation of the Nup192-Nup145N^{R1} interface through structure-guided mutagenesis confirmed the importance of the central hydrophobic Nup145N MYKL anchor motif (Fig.3F and fig.S18), but complete ablation of binding was only observed when the three flanking basic residues on either side were also mutated to alanine in the 10-residue KKR-MYKL-RKR mutant (Fig.3, F to H, and figs.S15, S18 to S20). Conversely, mutagenesis of the Nup145N^{R1} MYKL binding site in Nup192 identified a quadruple Nup192 LIFH mutant that specifically abolished Nup192 binding to Nup145N^{R1}, but not Nic96^{R2} or Nup53 (Fig.3, F and H, and figs.S19 to S21). Although basic residues flanking both Nup145N's MYKL and Nup53's FG (41) anchor motifs contribute to Nup192 binding, flanking residues were not resolved in the cryo-EM density.

Nup188 interaction with Nup145N.—To identify the Nup145N regions necessary and sufficient for Nup188 binding, we employed a five-alanine scanning and fragment truncation approach analogous to the mapping of the Nup145N-Nup192 interaction. This identified a minimal Nup145N^{R2} peptide (residues 640–732) that recapitulated wildtype binding, and a region between residues 706–715 that affected Nup188^{NTD} binding upon five-alanine substitution (Fig.4, A and B, and figs.S22 and S23). Consistent with our previous findings (28), we also confirmed that Nup188 does not bind Nup53, even in the presence of Nic96^{R2} and Nup145N (fig.S24).

We determined the structure of an ~220kDa Nup188•Nic96^{R2}•Nup145N^{R2} complex by single particle cryo-EM. An initial set of 709,123 preferentially oriented particles produced a reconstruction of Nup188•Nic96^{R2} at 2.4Å global resolution, and an anisotropic 2.3–2.5Å directional FSC resolution range. Local 3D classification of particles based on emergent excess density at the top of the question mark-shaped Nup188 molecule identified a subset of 298,317 particles that yielded a reconstruction of Nup188•Nic96^{R2}•Nup145N^{R2} at 2.8Å global resolution, and an anisotropic 2.7–2.9Å directional FSC resolution range (Fig.4C and fig.S25). Nup145N^{R2} buries residues I709, L710 and F715 in a hydrophobic cradle adjacent to the SH3-like domain. As with Nup145N^{R1} bound to Nup192, only a central portion of the Nup145N^{R2} peptide was resolved (residues 706–718) (Fig.4C). No significant conformational changes were observed between the different Nup188 structures, in response to linker binding (fig.S26).

Substitution of two resolved Nup145N residues, L710A and F715A, moderately disrupted Nup188^{NTD} binding (Fig.4D and fig.S27). Further systematic mutagenesis led to a Nup145N EDSILF mutant, which respectively abolished and reduced Nup188 binding to Nup145N^{R2} and Nup145N (Fig.4, E and F, and figs.S28 to S30). Structure-guided mutagenesis of Nup188 residues interfacing with Nup145N^{R2} identified a Nup188 HHMI mutant that abolished binding to Nup145N^{R2}, but not to Nup145N (Fig.4, D to F, and figs.S28 to S30). Overall, the greater tolerance of the Nup188-Nup145N interaction to binding site mutations demonstrates an even greater reliance on promiscuous binding events in flanking regions dispersed well beyond the structurally resolved core anchor motif.

Comparison of the Nup192- and Nup188-linker complexes.—The determination of full-length structures of both Nup192 and Nup188 scaffolds bound to their respective linkers permits a direct comparison of these two distantly homologous α-helical solenoids (~28% sequence similarity) (Movie 1). Although both structures share the same overall question mark-shaped architecture, the Nup188 α-helical solenoid displays a tighter super-helical twist, resulting in an ~10Å narrower molecule with a compacted N-terminal ring (fig.S31, A and B). A Tower protrudes from the midpoint of the α-helical solenoid towards the Head subdomain in both structures, extending further in Nup192 than the comparatively compressed Nup188 version. Nic96^{R2} binds both scaffolds at the base of the question mark, but remarkably adopts different secondary structures, switching between which requires breaking and re-forming of α-helices (fig.S31C). In contrast, Nup145N binds to different parts of Nup192 and Nup188, at the midpoint and the top of the question mark-shaped molecules, respectively. Interestingly, the Nup145N^{R2} binding site at the top of Nup188 is nearly congruent with that of the Nup53^{R1} on Nup192 (fig.S31A).

Our structures and biochemical analysis identify two distinct types of linker-scaffold interactions. Nic96^{R2} binds with high affinity, utilizing the same well-defined ~60-residue motif in binding to both Nup192 and Nup188. On the contrary, Nup145N binds to Nup192 and Nup188 through protracted, overlapping binding regions and a distinctive common binding mode: both interactions depend on a structurally defined ~10-residue Nup145N anchor motif, yet tight binding requires extensive ~20–60-residue N- and C-terminal flanking regions with high basic character. The Nup53-Nup192 interaction relies on a similar binding mode. The evasiveness of these interaction-enhancing linker flanking regions to structural characterization suggests that their binding to scaffold surfaces is highly dynamic and promiscuous. Notably, the previously characterized ~14-residue Nup170-binding motif of Nup145N (residues 729–750) does not depend on binding-enhancing flanking regions, suggesting that the uncovered Nup145N/Nup53 mode of binding to the Nup192 and Nup188 scaffolds is a desirable evolutionary outcome and architectural principle of the NPC inner ring.

Together, these data complete the structural and biochemical characterization of the biochemically tractable linker-scaffold interactions. Nup145N binds at distinct sites on Nup192 and Nup188, forming mutually exclusive interactions with either Nup192 and Nup170 or Nup188, through extensive overlapping binding sites mapped to Nup192 (R1, 616–683), Nup188 (R2, 640–732) and Nup170 (R3, 729–750). Binding via a central anchor motif enhanced by extensive flanking regions is reminiscent of Velcro, in which weak binding events accumulate to build a robust yet flexible interaction with manifold productive binding configurations possible in terms of both spatial distribution and occupancy. As an architectural principle, Velcro-like binding could accommodate scaffold movements without entirely breaking the linker-scaffold, maintaining the NPC's integrity in face of large-scale dilation or constriction.

Architecture of the *S.cerevisiae* linker-scaffold

The inner ring of the NPC contains eight-fold rotational symmetry about a nucleocytoplasmic axis and two-fold symmetry in the plane of the nuclear envelope (34, 35). In the *S.cerevisiae* NPC, each of the 16 inner ring protomers were proposed to consist of a *sc*Nup192 and a *sc*Nup188 IRC (Fig.1, C and D), with *sc*Nup192 and *sc*Nup188 located at the equatorial and peripheral positions, respectively (36, 37). High-confidence quantitative docking of our full-length experimental Nup192•Nic96^{R2}•Nup145N^{R1}•Nup53^{R1} and Nup188•Nic96^{R2}•Nup145N^{R2} structures in an ~25Å *in situ* cryo-ET map of the *S.cerevisiae* NPC (fig.S32) (36) confirmed these proposals. Whereas docking of the folded scaffolds Nup170, Nic96, Nup192, Nup188, and the CNT into cryo-ET maps of intact NPCs revealed their positioning to form four concentric cylinders, the linker network that connects them has remained elusive. Combined with our previously determined structures of Nup170•Nup53^{R3}, Nup170•Nup145N^{R3}, Nic96•Nup53^{R2}, and CNT•Nic96^{R1} (28, 35), the Nup192•Nic96^{R2}•Nup145N^{R1}•Nup53^{R1} and Nup188•Nic96^{R2}•Nup145N^{R2} structures allowed us to identify the locations of all scaffold-bound linker regions. We considered whether the length of linker polypeptides connecting pairs of scaffold-bound linker segments constrained the topology of linker connections. We found a single topology connecting linker segments related by the shortest Euclidean distance. For a detailed description of these results, see Supplementary Text (figs.S32 to S37).

Together, these data elucidated the architecture of the *S.cerevisiae* inner ring linker-scaffold (Fig.5A and Movie 2). Apart from spoke bridging mediated by Nup53 orthologs, all linker-scaffold connections in the *S.cerevisiae* inner ring occur within the same spoke, thereby allowing inter-spoke gaps to form. The linker-scaffold architecture provides a molecular explanation for the inner ring's ability to exist in constricted and dilated states (36, 37).

S.cerevisiae linker-scaffold is robust and essential

Due to ancestral gene duplication events in *S.cerevisiae*, there are several linker and scaffold nup paralogs, including *sc*Nup145N paralogs *sc*Nup116 and *sc*Nup100, *sc*Nup53 paralog *sc*Nup59, and *sc*Nup170 paralog *sc*Nup157 (Fig.1B) (2). The *sc*Nup100 and *sc*Nup116 paralogs contain sequences homologous to the Nup192, Nup188, and Nup170 binding regions characterized in *C.thermophilum* Nup145N, but only *sc*Nup116 possesses the Gle2 binding site (GLEBS) motif (fig.S38) (50).

To interrogate the function of individual scaffold-binding regions in the linker *sc*Nup116, we established a *S.cerevisiae* minimal *nup100Δnup116Δnup145Δ* strain complemented with *sc*Nup116 and *sc*Nup145C, ectopically expressed from centromeric plasmids (Fig.5, B and C, and fig.S39). Next, we systematically mutated all functional elements in the *sc*Nup116 sequence, including the *sc*Nup192, *sc*Nup188, and *sc*Nup157/170 scaffold-binding regions R1, R2, and R3, respectively, with three types of mutations: deletions (*ΔR1*, *ΔR2*, and *ΔR3*), substitutions with glycine-serine (GS)-linkers of equivalent length (*R1/40×GS*, *R2/40×GS*, and *R3/12×GS*), or substitutions of sequence-conserved residues shown to disrupt binding *of the C.thermophilum* Nup145N to the respective scaffolds (*R1m*, *R2m*, and *R3m*) (Fig.5B and fig.S38). Deletions and GS-linker-substitutions, being aggressive types of mutations, were lethal if targeting R1, and impacted growth and mRNA/60S pre-ribosome export if introduced in R2 and R3. The less aggressive combination of substitutions, *R1m,* caused significant yet non-lethal phenotypic effects, which were further exacerbated through combination with *R2m* (*R1m+R2m*) or *R3m* (*R1m+R3m*), culminating with the lethal *R1m+R2m+R3m* triple mutation (Fig.5, D to E and fig.S40). Interestingly, all *sc*Nup116 mutations resulted in temperature-dependent loss of eGFP-*sc*Nup116 from the nuclear envelope rim and concomitant emergence of eGFP-*sc*Nup116 foci (Fig.5D and fig.S40F), as previously reported (51–53).

Next, we transposed the insight from our structural and biochemical characterization of the *C.thermophilum* linker-scaffold into equivalent substitutions of conserved residues or more aggressive truncations of binding site-harboring subdomains of *sc*Nup192, *sc*Nup188, and *sc*Nic96 (Fig.5F). Remarkably, the combination of *LAF* and *LIFH* substitutions (*LAF+LIFH*) that ablated Nup192 binding to Nic96^{R2} and Nup145N^{R1}, respectively, failed to rescue the lethal *nup192Δ* phenotype (Fig.5G, and fig.S41 and S42). Analogously, the combination of *FLV* and *HHMI* substitutions (*FLV+HHMI*) that ablated Nup188 binding to Nic96^{R2} and Nup145N^{R2}, respectively, led to an additive cold-sensitive slow growth phenotype with mRNA/60S pre-ribosome export defects in the synthetic lethal *nup188Δpom34Δ* strain (Fig.5, G and H, and figs.S43 and S44) (54–56). Finally, we introduced the transposed *FFF* substitutions of evolutionarily conserved hydrophobic residues that abolished Nic96^{R2} binding to Nup192 and Nup188 into *sc*Nic96, along with *sc*Nic96^{R2} deletion (*ΔR2*) (Fig.5F and fig.S45). Surprisingly, neither mutation resulted in a significant phenotype in a *nic96Δ* strain (Fig.5, F to H and fig.S46). The composite structure of the NPC linker-scaffold suggests that Nic96^{R2} binding to Nup192 and Nup188 restricts the diffusive path of the N-terminal Nic96 linker, thereby correctly positioning the Nic96^{R1} assembly sensor that recruits the CNT complex (Fig.5J). We reasoned that CNT mispositioning would affect the spatial distribution and local concentration of FG repeats, with consequences on nucleocytoplasmic transport. Therefore, we replaced the Nic96^{R2} region with GS-linkers matching the number of residues (*R2/66×GS*) or approximating its α-helical length (*R2/32×GS*) (Fig.5F). Despite not affecting CNT recruitment by the Nic96^{R1} region, the *R2/66×GS* and *R2/32×GS* mutations respectively resulted in lethal and severely deleterious effects on growth and mRNA/60S pre-ribosome export (Fig.5, G to I, and fig.S46). For a detailed description of these results, see Supplementary Text.

Taken together, these data demonstrate the physiological relevance of our residue-level biochemical and structural characterization of Nup192 and Nup188 as keystone scaffold hubs of the inner ring that integrate connections between the membrane-coating Nup170 layer and the central transport channel-interfacing CNT layer through respective interactions with Nup145N and the N-terminal Nic96 linker regions. The wildtype phenotype of the *nup53Δnup59Δ* strain (57) precludes analysis of the *sc*Nup53/*sc*Nup59 interactions in *S.cerevisiae*. However, this fact coupled with our knockout of all but one of the *sc*Nup145N paralogs highlight the robustness of the *S.cerevisiae* inner ring architecture, which can tolerate a considerable loss of linker-scaffold interactions. Robustness is also found in nup-nup interactions, whereby perturbing a linker-scaffold interaction requires multiple residue substitutions in both structured motifs and flanking linker regions.

Evolutionary conservation of the human linker-scaffold

Despite low sequence conservation, composite structures of the human and *S.cerevisiae* NPC reveal an identical positioning of the scaffold nups, suggesting that the linker-scaffold architecture is evolutionarily conserved (34–37). Specifically, the human linker-scaffold interactions, the topology of scaffold-binding regions in the linkers, and the location of linker-binding sites in the scaffolds are expected to match those of the *C.thermophilum* nups (28, 33, 35, 40, 41). We developed expression and purification protocols for recombinant human nups (Fig.6A), enabling systematic interaction analyses between scaffold and linker nups, for which we generated truncation and sequence variants, aided by multispecies sequence alignments (figs.S38, S45, and S47 to S49). For a detailed description of these results, see Supplementary Text (figs.S50 to S53).

Together with our previous mapping of the NUP155^{CTD}-NUP98^{R3} interaction (35), these data establish that the linker-scaffold is evolutionarily conserved from *C.thermophilum* to humans, including the linker-binding sites in the scaffolds and the topology of the scaffold-binding regions in the linkers (fig.6B).

Biochemical and structural analysis of the human NUP93-NUP53 interaction

Our dissection of the human linker-scaffold interaction network identified an interaction between NUP93^{SOL} and a NUP53 region N-terminal of the RRM-like domain (residues 1–169; N) (fig.S51) that was nevertheless devoid of homology to the corresponding *C.thermophilum* Nup53^{R2} amphipathic α-helix motif that fits into a hydrophobic groove of the Nic96^{SOL} scaffold (figs.S48 and S49) (35). Through fragment truncation and five-alanine scanning mutagenesis, we identified a NUP53^{R2} region (residues 84–150) that formed a stable complex with NUP93^{SOL}, within which residues 86–100 were required for binding to NUP93^{SOL} (Fig.6, C and D, and figs.S54 and S55).

To elucidate the molecular details of binding between the divergent NUP53^{R2} and NUP93^{SOL}, we determined crystal structures of *apo* NUP93^{SOL} and NUP93^{SOL}•NUP53^{R2} at 2.0Å and 3.4Å resolution, respectively. As with other linker-scaffold interactions, only a core region (residues 88–95) of the biochemically mapped minimal NUP53^{R2} was resolved (Fig.6E and fig.S56). *C.thermophilum* and human Nic96^{SOL} orthologs display equivalent α-helical solenoid architectures (Fig.6F) (35, 58, 59). In contrast to the *C.thermophilum* Nup53^{R2} amphipathic α-helix, human NUP53^{R2} binds the conserved NUP93^{SOL} hydrophobic groove encompassing α-helices α5 and α13–15 as a linear eight-residue motif, burying ~1,100Å^2 of combined surface area (Fig.6, E and I to K, fig.S56E, and Movie 3). Systematic alanine substitution of the resolved NUP53^{R2} motif, invariant across metazoan NUP53 sequences (fig.S49), confirmed the key role of the P89-P90 di-proline and I94, consequently also illustrating the importance of the NUP93^{SOL} residues that interface with them (Fig.6, G, H, and L, and fig.S57).

Together, our data establish that despite distinct binding modes and low sequence conservation, linker-scaffold interactions are evolutionarily conserved, further highlighting their essential role and indicating that shape conservation of scaffolds is a key determinant of the NPC architecture.

Architecture of the human NPC symmetric core

Quantitative docking of nup complexes in cryo-ET maps of the human NPC.—We have previously demonstrated that nup ortholog crystal structures can be successfully used to interpret the density of an ~23Å cryo-ET map of the intact human NPC, yielding a near-atomic composite structure of the NPC symmetric core that included linker-scaffold crystal structures of the Nup170•Nup53^{R3}•Nup145N^{R3}, Nic96^{SOL}•Nup53^{R2}, and CNT•Nic96^{R1} complexes (28, 35). The newly available structures of full-length Nup192 and Nup188 as part of Nup192•Nic96^{R2}•Nup145N^{R1}•Nup53^{R1} and Nup188•Nic96^{R2}•Nup145N^{R2} linker-scaffold complexes, as well as the human NUP93^{SOL}•NUP53^{R2} complex, allowed us to build on our previous analysis with an improved ~12Å cryo-ET map of the intact human NPC (provided by Martin Beck's group) (47). As for the *S.cerevisiae* NPC described above, our quantitative docking approach consisted of statistically scoring the fit of resolution-matched densities simulated from crystal and single particle cryo-EM structures that were randomly placed and locally refined in cryo-ET maps of the human NPC. Structures of the CNC, Nup192•Nic96^{R2}•Nup145N^{R1}•Nup53^{R1}, Nup188•Nic96^{R2}•Nup145N^{R2}, and NUP358^{NTD} (reported in the accompanying manuscript) (60) were readily placed in cryo-ET maps of the entire NPC or of the inner ring portion. Assigned density was then iteratively subtracted from the maps to reduce the subsequent search space for NUP93^{SOL}•NUP53^{R2}, Nup170•Nup53^{R3}•Nup145N^{R3}, CNT•Nic96^{R1}, and NUP53^{RRM} (fig.S58). For a detailed description of these results, see Supplementary Text (figs.S58 to S77).

The structures and improved cryo-ET map of the intact human NPC have disambiguated the placement of NUP188 and NUP205 hubs in the inner ring and distal outer ring positions, led to the discovery of a proximal NUP205 in the cytoplasmic outer ring, identified NUP93^{SOL} in the outer rings, placed NUP53^{RRM} homodimers between inner ring spokes, and revealed a comprehensive map of scaffold-bound linker segments that implied a single symmetric core linker topology connecting linker segments related by the shortest Euclidean distance (figs.S77, S78, and Movie 4). The composite structure includes ~400,000 ordered residues that explain nearly all protein density of the symmetric core and assign the protein identity and location of ~64MDa out of ~110MDa of the human NPC mass.

Architecture of cytoplasmic and nuclear outer rings.—In both the cytoplasmic and nuclear outer rings of the human NPC, 16 copies of the Y-shaped CNC are arranged in two concentric proximal and distal rings. At equivalent locations on both cytoplasmic and nuclear sides, eight copies of NUP205 are intercalated between the proximal NUP75 arms and distal NUP107 stalks of CNCs from adjacent spokes. Eight NUP93^{SOL} copies are inserted between the distal NUP107 and proximal NUP96 α-helical solenoids, bisecting the stalks of tandem-arranged CNCs of a single spoke (Fig.7 and fig.S79). Stretched out, the ~25 residue unstructured linker connecting the R2 and SOL regions of NUP93 bridge the ~95Å gap between the distal NUP205-bound NUP93^{R2} and the distal NUP93^{SOL} of an adjacent spoke, thus crosslinking the outer ring spokes (Fig.7, figs.S78 to S80, and Movie 4). Compared to the Nup192 ortholog, NUP205 presents an additional ~240 residues that elongate the C-terminal Tail region, suggesting that ~95Å is an upper estimate for the distance between distal NUP93^{R2} and NUP93^{SOL} from adjacent spokes.

Unique to the cytoplasmic face, an additional eight copies of the proximal NUP205 are lodged between the NUP75 arm of the proximal CNC and the bridge NUP155 that connects the outer and inner ring (Fig.7A and fig.S79). The proximal NUP205-bound NUP93^{R2} can only be linked with a proximal NUP93^{SOL} of the same spoke (Fig.7A and figs.S79 and S80A). Furthermore, the arrangement of NUP53 binding sites on NUP93^{SOL} and NUP205 copies in the cytoplasmic outer rings is compatible with the NUP53-mediated linkage of the distal NUP205 with the proximal NUP93^{SOL} and, conversely, the proximal NUP205 with the distal NUP93^{SOL} (Fig.7 and figs.S79 and S80, D and E). NUP53 could also mediate long-range links between the bridge NUP155 and the R1 and R2 binding sites on outer ring NUP205 and NUP93^{SOL}, respectively (fig.S80, F, H and I).

On both nuclear and cytoplasmic sides, the NUP98^{APD}-binding NUP96 sites present in the 16 CNC copies recruit 16 copies of NUP98 that can simultaneously satisfy the outer ring NUP205 binding sites due to the ~115-residue linker between the APD and the R1-R2-R3 regions (Fig.7 and fig.S79). The cytoplasmic proximal NUP205 and bridge NUP155 scaffolds could in principle be linked by NUP98, although NUP98^{R3} is likely outcompeted from its bridge NUP155 binding site by the asymmetric cytoplasmic filament nups GLE1•NUP42 (61), as explained in the accompanying manuscript (Fig.7A and fig.S80C) (60). To maximize nup copy parsimony while satisfying all available scaffold binding sites, the outer rings would recruit 16 copies of NUP53 and NUP98 on each side of the NPC.

Architecture of the inner ring linker-scaffold.—The quantitative docking confirmed evolutionary conservation of the inner ring linker-scaffold architecture between *H.sapiens* and *S.cerevisiae* NPCs (Fig.8). A NUP155•NUP53 linker-scaffold coats the nuclear envelope, anchored by membrane curvature-sensing ALPS motifs and the C-terminal NUP53 amphipathic helix (35, 62–64), with a peripheral and equatorial copy on each side of a spoke midplane. The homodimerizing NUP53^{RRM} domains link spoke halves across the midplane (Fig.8C and figs.S81 and S82, A and B). A second cross-midplane link between NUP53 and NUP93 connects NUP188•NUP93•CNT and NUP205•NUP93•CNT modules to the NUP155 coat at equatorial and peripheral positions, respectively (Fig.8, D to F, and fig.S82, C to J). Restrained by their length, NUP93 N-terminal linkers connect NUP188 with the peripheral, and NUP205 with the equatorial inner ring NUP93^{SOL} and CNT copies of the same inner ring spoke (Fig.8, D to F, and fig.S82, G to J).

The equatorial position of NUP205 is further solidified by a NUP98-mediated linkage with the equatorial NUP155 and by a NUP53-mediated linkage with a peripheral NUP93 from an adjacent spoke (Fig.8E and fig.S82, E and F). As in the *S.cerevisiae* NPC, the NUP205, NUP188, and peripheral NUP155 binding sites for the NUP98 R1, R2, and R3 regions, respectively, are too far apart to be linked by the same NUP98, suggesting that three NUP98 copies are required to satisfy all binding sites on each side of a spoke midplane instead. The NUP98^{APD}-binding NUP96 and cytoplasmic filament NUP88^{NTD} (placed in the accompanying manuscript) (60) sites are within reach of the ~115-residue linker between the APD and the R1-R2-R3 regions, thus linking the inner ring with the outer ring and cytoplasmic asymmetric portions of the NPC.

The inner ring scaffold architecture is remarkably interwoven by linker interactions (Movie 4). The peripheral NUP155-NUP188-NUP93-CNT and equatorial NUP155-NUP205-NUP93-CNT scaffold modules that together form a protomer for a D8-symmetric inner ring can themselves be superposed, if NUP188 and NUP205 are considered as equivalent organizing hubs (Fig.8G). Nevertheless, the peripheral NUP155 is not linked to the peripheral NUP188•NUP93•CNT complex from the same side of a spoke midplane. Instead, within each spoke, linker-mediated complexes form between a peripheral NUP188•NUP98•NUP93•CNT•NUP53 and an equatorial NUP155 from across the midplane (fig.S82K). On the contrary, the equatorial NUP205•NUP98•NUP93•CNT•NUP53 complex is linked with a peripheral NUP155 from the same and an equatorial NUP155 from the opposite side of a spoke midplane, through NUP98- and NUP53-mediated links, respectively (fig.S82K).

To maximize nup copy parsimony while satisfying all available scaffold binding sites, the human NPC would recruit a total 56 and 80 copies of NUP53 and NUP98, respectively. Though the rest of the symmetric core composite structure agrees with previous estimates of nup stoichiometry, the implied NUP98 and NUP53 copy number exceeds the empirical measurements (65). Whereas the discrepancy may be explained by available NUP98 and NUP53 binding sites not being fully occupied, the NUP98 and NUP53 linker nups are known to exchange comparatively rapidly at the NPC (66, 67), and might get depleted as part of the preparation for mass spectrometric analysis.

Docking the composite structure of the NPC into a ~37Å *in situ* cryo-ET map of the dilated human NPC revealed that the inner ring spokes move as relatively rigid bodies, accommodating the dilation by increasing the NUP53 linker-bridged gaps between spokes (fig.S83, A and B) (45). Spatial restraints in the dilated NPC confirm the intra-spoke topology of linkages established by N-terminal NUP93 and NUP98 linkers. Remarkably, the dilation of the NPC does not induce a significant increase in the gap between the adjacent spokes of the outer rings, consistent with the crosslinking purported by the linker between distal NUP93 R2 and SOL regions of adjacent spokes (fig.S83B and Movie 5).

Conclusions

The linker-scaffold is a fundamental architectural principle of the NPC structure. Despite the continuing improvement in resolution attained by cryo-ET reconstructions of intact NPCs over the last decade, the fine molecular detail of the linker-scaffold has remained out of reach. We employed comprehensive residue-level biochemical reconstitution and mapping, crystallographic and single particle cryo-EM structure determination, *in vivo* validation, and quantitative docking into improved and diversified cryo-ET NPC reconstructions to delineate the near-atomic structure and evolutionary conservation of the linker-scaffold interactions that underpin the integrity of the NPC.

This study completes the set of structures capturing all biochemically tractable linker-scaffold interactions of the symmetric core. Docked into cryo-ET maps of the human and *S.cerevisiae* NPC, they reveal the topology and restrain distances between linker binding sites on scaffold surfaces, outlining how the multivalent linkers Nup145N/NUP98, Nup53/

NUP53 and the N-terminal region of Nic96/NUP93 connect different parts of the NPC. Linkers mediate the formation of inner ring complexes that coalesce into relatively rigid spokes spanning from the nuclear envelope to the central transport channel. They also cross-stitch the inner ring scaffolds with connections across spoke midplanes and flexible links between spokes. In the outer rings, linker-scaffold interactions connect spokes and project ties towards the inner ring.

Our biochemical analysis of linker-scaffold interactions involving Nup145N and Nup53 revealed another architectural principle, invisible to structural methods: linker-scaffold interactions are driven by structurally defined anchor motifs that present canonical two-component binding dynamics, but are potentiated by disperse, structurally elusive interactions between flanking residues and promiscuous binding sites on scaffold surfaces. These Velcro-like binding modes, sometimes referred to as ‘fuzzy interactions,’ are found in systems involving intrinsically disordered proteins across biology, a prominent example being the ultrafast exchange of nucleocytoplasmic transport receptors on FG repeats (12).

The physical and chemical properties of linkers are advantageous for the assembly of giant complexes like the NPC. The unfolded property of linkers enables long-range interactions and confers flexibility that can accommodate large movements or shock-absorb nuclear envelope deformations. The disperse nature of linker-scaffold interactions is conducive to the reuse of linker interactions in different chemical and steric environments of the NPC. The ensemble of binding modes provides robustness in the face of conformational changes of the NPC that might otherwise be incompatible with a singular binding mode. The bulk of FG repeats present in the central transport channel, which form promiscuous transient interactions with the inner ring scaffold and other parts of the NPC, is likely to have a similar effect. Specifically, the previous findings that FG repeats not only form the NPC’s diffusion barrier, but also interact with scaffolds, supports this notion (49, 52, 58, 68, 69). Considering the avidity that results from multiple scaffold valences per linker, and the allovalency mediated by flanking residues (70, 71), it is unsurprising that our *in vivo* perturbation of interactions required extensive mutations to exacerbate deleterious phenotypes. For this reason and because of the lack of constraints imposed by a protein fold, new linker sequences are readily evolvable. Remarkably, the linker-scaffold network topology and modular binding site distribution on linkers is conserved from fungi to humans, despite striking divergence in linker sequences, most extremely exemplified by the complete divergence of the Nup53/NUP53 motif that binds to a conserved site on Nic96/NUP93.

The binding of linkers is amenable to exchange and regulation. The linearity of linkers imposes few obstacles to the deposition of post-translational modifications by the same machinery along the entire sequence to rapidly ablate the multiple binding valences. Indeed, patterns of Cdk1 and Nek-driven phosphorylation that lead to the choreographed depletion of both NUP98 and NUP53 from the NPC during mitotic nuclear envelope breakdown include the R1, R2 and R3 regions of both linkers (72, 73). Structural defects in the NPC resulting in aberrant nucleocytoplasmic transport may affect gene expression, mRNA maturation and export, leading to downstream tumorigenic processes. Therefore, the depletion of NUP98 from the NPC as a result of gene fusion mutations associated with various hematopoietic malignancies should be considered in the study of the carcinogenic mechanisms triggered by these mutations (74).

The unexpected discovery of the presence and unique role of NUP93 in crosslinking the outer ring spokes of the human NPC, along with its organizing role in the inner ring as both scaffold and linker, exemplifies the reuse of linker-scaffold functional units at completely different locations of the NPC. Its ubiquity rationalizes the observation that rapid degron-induced depletion of NUP93 leads to the concomitant loss of both inner and outer rings from the nuclear pore, legitimizing NUP93 as a 'lynchpin' of the NPC (75). These findings further inform the mechanistic basis for pathologies like steroid-resistant nephrotic syndrome (SRNS), which is associated with mutations in NUP93 and NUP205, the most poignant of which is NUP205 F1995S, located in the NUP93^{R2} binding site of NUP205 and shown to abolish the NUP205-NUP93 interaction (76). Nonsense mutations that omit the NUP93^{R2} binding site in NUP188 are also associated with neurologic, ocular, and cardiac abnormalities (77).

The docking of our NPC composite structure into an ~37Å *in situ* cryo-ET map of the dilated human NPC demonstrates the magnitude of the movements that must be withstood by the linkers that connect the inner ring spokes (45). Importantly, the dilated inner ring reveals lateral channels between its spokes that can accommodate the passage of small cytosolic domains of inner nuclear membrane integral membrane proteins (INM-IMPs), suggesting the mechanism by which inner ring constriction upon energy depletion might interfere with the path of diffusion of these proteins between outer and inner nuclear envelope membranes (78–80). It remains to be established whether the extent of inner ring dilation observed by current cryo-ET reconstructions of the human and *S.cerevisiae* NPC capture the maximally achievable lateral channel dimensions. However, the previous observations that karyopherin-mediated active INM-IMP transport requires unstructured tethers spanning the distance between the nuclear envelope and the central transport channel is consistent with the observed lateral channel dimensions (fig.S83C) (81–85). Taking advantage of the composite NPC structures, future studies are expected to elucidate the nucleocytoplasmic translocation pathways and the impact of inner ring dilation for individual INM-IMPs. Similarly, the translocation of perinuclear domains on the opposite side of the nuclear envelope is expected to be limited by the luminal ring that encircles the NPC midplane formed by Pom152/POM210 Ig-like domains (37, 47, 86).

Finally, the capacity of the NPC to exist in dilated and constricted states dependent on tension imparted by the surrounding nuclear envelope portrays the NPC as the cell's largest mechanosensitive channel, with implications in cellular energy state sensing and transport of transcriptional regulators in response to mechanical stress on the cell (46, 87). The constriction and dilation of the inner ring may affect the distribution and local concentration of FG repeats in the central transport channel, a determinant of karyopherin-mediated transport efficiency (88), but also sterically modulate the flux of INM-IMPs and large cargos such as pre-ribosome or messenger ribonucleoprotein particles (mRNPs). Future studies will have to establish the causal links between the transmission of tension from the nuclear envelope to the NPC, the dilation of its inner ring, and mechanisms by which dilation and constriction may modulate nucleocytoplasmic transport.

Our results shed light on the elusive linker-scaffold molecular interactions that maintain the integrity of the NPC, providing a comprehensive characterization of a final major aspect of the NPC symmetric core. Building on this roadmap, future studies can address NPC assembly and disassembly mechanisms, the emergence of NPC polarity and attachment of the asymmetric cytoplasmic filaments and nuclear basket to the symmetric core, mechanisms of NPC-associated diseases, and mechanisms of NPC dilation and constriction along with their implications in nucleocytoplasmic transport.

Methods Summary

Comprehensive Materials and Methods are presented in the Supplementary Materials. Briefly, the source of materials and reagents is listed in Table S1. Summaries of bacterial expression constructs and conditions (Table S2), protein purification procedures (Table S3), analytical size-exclusion chromatography coupled to inline multi-angle light scattering (SEC-MALS) protein interaction analyses (Table S4), and isothermal titration calorimetry (ITC) binding affinity measurements (Table S5), are provided. Experimental details of X-ray crystallography and single particle cryo-EM structure determination procedures are described, including summaries of crystallization and cryo-protection conditions (Table S6), as well as data collection, processing, and refinement statistics (Tables S7 to S12). *S.cerevisiae* constructs (Table S13) and strains (Table S14), as well as the experimental details of the viability and growth assay, subcellular nup localization analysis, 60S pre-ribosome export assay, and mRNA export fluorescence *in situ* hybridization (FISH) assay, which establish the physiological relevance of the biochemical and structural findings, are provided. Details of the incremental quantitative docking procedures for nup and nup complex crystal and single particle cryo-EM structures into ~12Å and ~23Å cryo-ET maps of the intact human NPC (constricted state) (38, 47), as well as into an ~37Å *in situ* cryo-ET map of the human NPC (45) and an ~25Å *in situ* map of the *S.cerevisiae* NPC (36) (dilated states), are provided. Inventories of nup and nup complex experimental structures used to generate the near-atomic composite structures of the *S.cerevisiae* (Table S15) and human (Table S16) NPCs, are provided.

Supplementary Material

Refer to Web version on PubMed Central for supplementary material.

Acknowledgements:

We thank Alina Patke for critical reading and editing of the manuscript and insightful discussions; Martin Beck for sharing an ~12Å cryo-ET reconstruction of the intact human HeLa cell NPC prior to publication (EMD-14322); Ed Hurt, Susan Wente, Beatriz Fountura, David Baltimore and the Kazusa DNA Research Institute for providing material, and Felice Liang, Alex Lyons, Aaron Tang, and Jimmy Thai for experimental support. We are grateful to Dominika Borek, Justin Kollman, Gabe Lander, Daniel Lin, Shyam Saladi, and members of the Hoelz lab for insightful discussion and expertise. We acknowledge Jens Kaiser, the scientific staff of the SSRL beamline 12–2, and the National Institute of General Medical Sciences and National Cancer Institute Structural Biology Facility (GM/CA) at the Advanced Photon Source (APS) for their support with X-ray diffraction measurements; Songye Chen and Andrey Malyutin of the Beckman Institute Resource Center for Transmission Electron Microscopy at the Caltech for support with cryo-electron microscopy imaging; Janette Myers and the scientific staff of the Pacific Northwest CryoEM Center (PNCC) at the Oregon Health and Science University (OHSU) and the Environmental Molecular Sciences Laboratory (EMSL) for their support with cryo-EM imaging; the Cold Spring Harbor Laboratory (CSHL) cryo-EM course, the CSHL X-ray Methods in Structural Biology course, and the Michigan Life Science Institute cryo-EM workshop and their instructors Michael Cianfrocco, William Furey, Gary

Gilliland, Justin Kollman, Gabe Lander, Melanie Ohi, James Pflugrath, Alexander McPherson, and Matthijn Vos, along with and all the course staff and lecturers for valuable expert training.

Funding:

The Molecular Observatory at the California Institute of Technology (Caltech) is supported by Donald and Judith Voet, the Gordon and Betty Moore Foundation, and the Beckman Institute. The Center for Molecular Medicine at Caltech is supported by the Gordon and Betty Moore Foundation. The operations at the SSRL and APS are supported by the U.S. Department of Energy and the National Institutes of Health (NIH). GM/CA has been funded in whole or in part with federal funds from the National Cancer Institute (ACB-12002) and the National Institute of General Medical Sciences (AGM-12006). A portion of this research was supported by NIH grant U24GM129547 and performed at the PNCC at OHSU and accessed through EMSL (grid.436923.9), a DOE Office of Science User Facility sponsored by the Office of Biological and Environmental Research. AH was supported by a Camille-Dreyfus Teacher Scholar Award (TC-15–082) and NIH grants R01-GM117360 and R01-GM111461, is an Investigator of the Heritage Medical Research Institute (HMRI-15–09-01), and a Faculty Scholar of the Howard Hughes Medical Institute (55108534). SP was supported by a pre-doctoral fellowship from the Boehringer Ingelheim Fonds and by an Amgen Graduate Fellowship through the Caltech-Amgen Research Collaboration.

Data and materials availability:

Materials generated in this study are available on request from the corresponding author. The coordinates and structure factors of crystal structures have been deposited in the PDB with accession numbers 7MVT (Nup192$^{\Delta\text{Head}}$•Nic96$^{187–301}$), 7MVW (Nup188$^{\text{NTD}}$), 7MVX (Nup188•Nic96$^{\text{R2}}$), 7MW0 (NUP93$^{\text{SOL}}$), and 7MW0 (NUP93$^{\text{SOL}}$•NUP53$^{\text{R2}}$). The coordinates of single particle cryo-EM structures have been deposited in the PDB with accession numbers 7MVU (Nup192•Nic96$^{\text{R2}}$), 7MVV (Nup192•Nic96$^{\text{R2}}$•Nup145N$^{\text{R1}}$•Nup53$^{\text{R1}}$), 7MVY (Nup188•Nic96$^{\text{R2}}$), and 7MVZ (Nup188•Nic96$^{\text{R2}}$•Nup145N$^{\text{R2}}$). The maps of single particle cryo-EM structures have been deposited in the EMDB with accession numbers EMD-24056 (Nup192•Nic96$^{\text{R2}}$), EMD-24057 (Nup192•Nic96$^{\text{R2}}$•Nup145N$^{\text{R1}}$•Nup53$^{\text{R1}}$), EMD-24058 (Nup188•Nic96$^{\text{R2}}$), EMD-24059 (Nup188•Nic96$^{\text{R2}}$•Nup145N$^{\text{R2}}$). PyMol and Chimera sessions containing the composite structures of the constricted human, dilated human, and dilated *S.cerevisiae* NPC symmetric core can be obtained from our webpage (http://ahweb.caltech.edu) and coordinates are deposited in the PDB with the respective accession numbers 7TBJ, 7TBK, and 7TBI. Quantitative docking data, workflow code, PyMol and Chimera sessions were deposited on CaltechDATA (89).

References and Notes:

1. Hoelz A, Debler EW, Blobel G, The structure of the nuclear pore complex. Annu. Rev. Biochem. 80, 613–643 (2011). [PubMed: 21495847]
2. Lin DH, Hoelz A, The Structure of the Nuclear Pore Complex (An Update). Annu. Rev. Biochem. 88, 725–783 (2019). [PubMed: 30883195]
3. Hampoelz B, Andres-Pons A, Kastritis P, Beck M, Structure and Assembly of the Nuclear Pore Complex. Annu. Rev. Biophys. 48, 515–536 (2019). [PubMed: 30943044]
4. Knockenhauer KE, Schwartz TU, The Nuclear Pore Complex as a Flexible and Dynamic Gate. Cell 164, 1162–1171 (2016). [PubMed: 26967283]
5. Kohler A, Hurt E, Gene regulation by nucleoporins and links to cancer. Mol. Cell 38, 6–15 (2010). [PubMed: 20385085]
6. Yarbrough ML, Mata MA, Sakthivel R, Fontoura BM, Viral subversion of nucleocytoplasmic trafficking. Traffic 15, 127–140 (2014). [PubMed: 24289861]
7. Paine PL, Moore LC, Horowitz SB, Nuclear envelope permeability. Nature 254, 109–114 (1975). [PubMed: 1117994]

8. Bonner WM, Protein migration into nuclei. I. Frog oocyte nuclei in vivo accumulate microinjected histones, allow entry to small proteins, and exclude large proteins. J. Cell Biol. 64, 421–430 (1975). [PubMed: 46868]
9. Timney BL, Raveh B, Mironska R, Trivedi JM, Kim SJ, Russel D, Wente SR, Sali A, Rout MP, Simple rules for passive diffusion through the nuclear pore complex. J. Cell Biol. 215, 57–76 (2016). [PubMed: 27697925]
10. Chook YM, Suel KE, Nuclear import by karyopherin-betas: recognition and inhibition. Biochim. Biophys. Acta 1813, 1593–1606 (2011). [PubMed: 21029754]
11. Cook A, Bono F, Jinek M, Conti E, Structural biology of nucleocytoplasmic transport. Annu. Rev. Biochem. 76, 647–671 (2007). [PubMed: 17506639]
12. Milles S, Mercadante D, Aramburu IV, Jensen MR, Banterle N, Koehler C, Tyagi S, Clarke J, Shammas SL, Blackledge M, Grater F, Lemke EA, Plasticity of an ultrafast interaction between nucleoporins and nuclear transport receptors. Cell 163, 734–745 (2015). [PubMed: 26456112]
13. Pumroy RA, Cingolani G, Diversification of importin-alpha isoforms in cellular trafficking and disease states. Biochem. J. 466, 13–28 (2015). [PubMed: 25656054]
14. Hodel AE, Hodel MR, Griffis ER, Hennig KA, Ratner GA, Xu S, Powers MA, The three-dimensional structure of the autoproteolytic, nuclear pore-targeting domain of the human nucleoporin Nup98. Mol. Cell 10, 347–358 (2002). [PubMed: 12191480]
15. Berke IC, Boehmer T, Blobel G, Schwartz TU, Structural and functional analysis of Nup133 domains reveals modular building blocks of the nuclear pore complex. J. Cell Biol. 167, 591–597 (2004). [PubMed: 15557116]
16. Hsia KC, Stavropoulos P, Blobel G, Hoelz A, Architecture of a coat for the nuclear pore membrane. Cell 131, 1313–1326 (2007). [PubMed: 18160040]
17. Boehmer T, Jeudy S, Berke IC, Schwartz TU, Structural and functional studies of Nup107/Nup133 interaction and its implications for the architecture of the nuclear pore complex. Mol. Cell 30, 721–731 (2008). [PubMed: 18570875]
18. Brohawn SG, Leksa NC, Spear ED, Rajashankar KR, Schwartz TU, Structural evidence for common ancestry of the nuclear pore complex and vesicle coats. Science 322, 1369–1373 (2008). [PubMed: 18974315]
19. Debler EW, Ma Y, Seo HS, Hsia KC, Noriega TR, Blobel G, Hoelz A, A fence-like coat for the nuclear pore membrane. Mol. Cell 32, 815–826 (2008). [PubMed: 19111661]
20. Brohawn SG, Schwartz TU, Molecular architecture of the Nup84-Nup145C-Sec13 edge element in the nuclear pore complex lattice. Nat. Struct. Mol. Biol. 16, 1173–1177 (2009). [PubMed: 19855394]
21. Leksa NC, Brohawn SG, Schwartz TU, The structure of the scaffold nucleoporin Nup120 reveals a new and unexpected domain architecture. Structure 17, 1082–1091 (2009). [PubMed: 19576787]
22. Nagy V, Hsia KC, Debler EW, Kampmann M, Davenport AM, Blobel G, Hoelz A, Structure of a trimeric nucleoporin complex reveals alternate oligomerization states. Proc. Natl. Acad. Sci. U.S.A. 106, 17693–17698 (2009). [PubMed: 19805193]
23. Seo HS, Ma Y, Debler EW, Wacker D, Kutik S, Blobel G, Hoelz A, Structural and functional analysis of Nup120 suggests ring formation of the Nup84 complex. Proc. Natl. Acad. Sci. U.S.A. 106, 14281–14286 (2009). [PubMed: 19706512]
24. Whittle JRR, Schwartz TU, Architectural nucleoporins Nup157/170 and Nup133 are structurally related and descend from a second ancestral element. J. Biol. Chem. 284, 28442–28452 (2009). [PubMed: 19674973]
25. Bilokapic S, Schwartz TU, Molecular basis for Nup37 and ELY5/ELYS recruitment to the nuclear pore complex. Proc. Natl. Acad. Sci. U.S.A. 109, 15241–15246 (2012). [PubMed: 22955883]
26. Bilokapic S, Schwartz TU, Structural and functional studies of the 252 kDa nucleoporin ELYS reveal distinct roles for its three tethered domains. Structure 21, 572–580 (2013). [PubMed: 23499022]
27. Kelley K, Knockenhauer KE, Kabachinski G, Schwartz TU, Atomic structure of the Y complex of the nuclear pore. Nat. Struct. Mol. Biol. 22, 425–431 (2015). [PubMed: 25822992]
28. Stuwe T, Bley CJ, Thierbach K, Petrovic S, Schilbach S, Mayo DJ, Perriches T, Rundlet EJ, Jeon YE, Collins LN, Huber FM, Lin DH, Paduch M, Koide A, Lu V, Fischer J, Hurt E, Koide S,

Kossiakoff AA, Hoelz A, Architecture of the fungal nuclear pore inner ring complex. Science 350, 56–64 (2015). [PubMed: 26316600]

29. Stuwe T, Correia AR, Lin DH, Paduch M, Lu VT, Kossiakoff AA, Hoelz A, Nuclear pores. Architecture of the nuclear pore complex coat. Science 347, 1148–1152 (2015). [PubMed: 25745173]
30. Xu C, Li Z, He H, Wernimont A, Li Y, Loppnau P, Min J, Crystal structure of human nuclear pore complex component NUP43. FEBS Lett. 589, 3247–3253 (2015). [PubMed: 26391640]
31. Hoelz A, Glavy JS, Beck M, Toward the atomic structure of the nuclear pore complex: when top down meets bottom up. Nat. Struct. Mol. Biol. 23, 624–630 (2016). [PubMed: 27273515]
32. Bui KH, von Appen A, DiGuilio AL, Ori A, Sparks L, Mackmull MT, Bock T, Hagen W, Andres-Pons A, Glavy JS, Beck M, Integrated structural analysis of the human nuclear pore complex scaffold. Cell 155, 1233–1243 (2013). [PubMed: 24315095]
33. Fischer J, Teimer R, Amlacher S, Kunze R, Hurt E, Linker Nups connect the nuclear pore complex inner ring with the outer ring and transport channel. Nat. Struct. Mol. Biol. 22, 774–781 (2015). [PubMed: 26344569]
34. Kosinski J, Mosalaganti S, von Appen A, Teimer R, DiGuilio AL, Wan W, Bui KH, Hagen WJ, Briggs JA, Glavy JS, Hurt E, Beck M, Molecular architecture of the inner ring scaffold of the human nuclear pore complex. Science 352, 363–365 (2016). [PubMed: 27081072]
35. Lin DH, Stuwe T, Schilbach S, Rundlet EJ, Perriches T, Mobbs G, Fan Y, Thierbach K, Huber FM, Collins LN, Davenport AM, Jeon YE, Hoelz A, Architecture of the symmetric core of the nuclear pore. Science 352, aaf1015 (2016). [PubMed: 27081075]
36. Allegretti M, Zimmerli CE, Rantos V, Wilfling F, Ronchi P, Fung HKH, Lee CW, Hagen W, Turonova B, Karius K, Bormel M, Zhang X, Muller CW, Schwab Y, Mahamid J, Pfander B, Kosinski J, Beck M, In-cell architecture of the nuclear pore and snapshots of its turnover. Nature 586, 796–800 (2020). [PubMed: 32879490]
37. Kim SJ, Fernandez-Martinez J, Nudelman I, Shi Y, Zhang W, Raveh B, Herricks T, Slaughter BD, Hogan JA, Upla P, Chemmama IE, Pellarin R, Echeverria I, Shivaraju M, Chaudhury AS, Wang J, Williams R, Unruh JR, Greenberg CH, Jacobs EY, Yu Z, de la Cruz MJ, Mironska R, Stokes DL, Aitchison JD, Jarrold MF, Gerton JL, Ludtke SJ, Akey CW, Chait BT, Sali A, Rout MP, Integrative structure and functional anatomy of a nuclear pore complex. Nature 555, 475–482 (2018). [PubMed: 29539637]
38. von Appen A, Kosinski J, Sparks L, Ori A, DiGuilio AL, Vollmer B, Mackmull MT, Banterle N, Parca L, Kastritis P, Buczak K, Mosalaganti S, Hagen W, Andres-Pons A, Lemke EA, Bork P, Antonin W, Glavy JS, Bui KH, Beck M, In situ structural analysis of the human nuclear pore complex. Nature 526, 140–143 (2015). [PubMed: 26416747]
39. Nordeen SA, Turman DL, Schwartz TU, Yeast Nup84-Nup133 complex structure details flexibility and reveals conservation of the membrane anchoring ALPS motif. Nat. Commun. 11, 6060 (2020). [PubMed: 33247142]
40. Amlacher S, Sarges P, Flemming D, van Noort V, Kunze R, Devos DP, Arumugam M, Bork P, Hurt E, Insight into structure and assembly of the nuclear pore complex by utilizing the genome of a eukaryotic thermophile. Cell 146, 277–289 (2011). [PubMed: 21784248]
41. Stuwe T, Lin DH, Collins LN, Hurt E, Hoelz A, Evidence for an evolutionary relationship between the large adaptor nucleoporin Nup192 and karyopherins. Proc. Natl. Acad. Sci. U.S.A. 111, 2530–2535 (2014). [PubMed: 24505056]
42. Chug H, Trakhanov S, Hulsmann BB, Pleiner T, Gorlich D, Crystal structure of the metazoan Nup62*Nup58*Nup54 nucleoporin complex. Science 350, 106–110 (2015). [PubMed: 26292704]
43. Mosalaganti S, Kosinski J, Albert S, Schaffer M, Strenkert D, Salome PA, Merchant SS, Plitzko JM, Baumeister W, Engel BD, Beck M, In situ architecture of the algal nuclear pore complex. Nat. Commun. 9, 2361 (2018). [PubMed: 29915221]
44. Schuller AP, Wojtynek M, Mankus D, Tatli M, Kronenberg-Tenga R, Regmi SG, Dip PV, Lytton-Jean AKR, Brignole EJ, Dasso M, Weis K, Medalia O, Schwartz TU, The cellular environment shapes the nuclear pore complex architecture. Nature, (2021).

45. Zila V, Margiotta E, Turonova B, Muller TG, Zimmerli CE, Mattei S, Allegretti M, Borner K, Rada J, Muller B, Lusic M, Krausslich HG, Beck M, Cone-shaped HIV-1 capsids are transported through intact nuclear pores. Cell 184, 1032–1046 e1018 (2021). [PubMed: 33571428]

46. Zimmerli CE, Allegretti M, Rantos V, Goetz SK, Obarska-Kosinska A, Zagoriy I, Halavatyi A, Hummer G, Mahamid J, Kosinski J, Beck M, Nuclear pores dilate and constrict in cellulo. Science 374, eabd9776 (2021). [PubMed: 34762489]

47. Mosalaganti S, Obarska-Kosinska A, Siggel M, Turonova B, Zimmerli CE, Buczak K, Schmidt FH, Margiotta E, Mackmull M-T, Hagen W, Hummer G, Beck M, Kosinski J, Artificial intelligence reveals nuclear pore complexity. bioRxiv, 2021.2010.2026.465776 (2021).

48. Sampathkumar P, Kim SJ, Upla P, Rice WJ, Phillips J, Timney BL, Pieper U, Bonanno JB, Fernandez-Martinez J, Hakhverdyan Z, Ketaren NE, Matsui T, Weiss TM, Stokes DL, Sauder JM, Burley SK, Sali A, Rout MP, Almo SC, Structure, dynamics, evolution, and function of a major scaffold component in the nuclear pore complex. Structure 21, 560–571 (2013). [PubMed: 23499021]

49. Andersen KR, Onischenko E, Tang JH, Kumar P, Chen JZ, Ulrich A, Liphardt JT, Weis K, Schwartz TU, Scaffold nucleoporins Nup188 and Nup192 share structural and functional properties with nuclear transport receptors. Elife 2, e00745 (2013). [PubMed: 23795296]

50. Bailer SM, Siniossoglou S, Podtelejnikov A, Hellwig A, Mann M, Hurt E, Nup116p and nup100p are interchangeable through a conserved motif which constitutes a docking site for the mRNA transport factor gle2p. EMBO J. 17, 1107–1119 (1998). [PubMed: 9463388]

51. Ryan KJ, Wente SR, Isolation and characterization of new Saccharomyces cerevisiae mutants perturbed in nuclear pore complex assembly. BMC Genet. 3, 17 (2002). [PubMed: 12215173]

52. Patel SS, Belmont BJ, Sante JM, Rexach MF, Natively unfolded nucleoporins gate protein diffusion across the nuclear pore complex. Cell 129, 83–96 (2007). [PubMed: 17418788]

53. Yoshida K, Seo HS, Debler EW, Blobel G, Hoelz A, Structural and functional analysis of an essential nucleoporin heterotrimer on the cytoplasmic face of the nuclear pore complex. Proc. Natl. Acad. Sci. U.S.A. 108, 16571–16576 (2011). [PubMed: 21930948]

54. de Bruyn Kops A, Guthrie C, Identification of the Novel Nup188-brr7 Allele in a Screen for Cold-Sensitive mRNA Export Mutants in Saccharomyces cerevisiae. G3 (Bethesda) 8, 2991–3003 (2018). [PubMed: 30021831]

55. Miao M, Ryan KJ, Wente SR, The integral membrane protein Pom34p functionally links nucleoporin subcomplexes. Genetics 172, 1441–1457 (2006). [PubMed: 16361228]

56. Nehrbass U, Rout MP, Maguire S, Blobel G, Wozniak RW, The yeast nucleoporin Nup188p interacts genetically and physically with the core structures of the nuclear pore complex. J. Cell Biol. 133, 1153–1162 (1996). [PubMed: 8682855]

57. Marelli M, Aitchison JD, Wozniak RW, Specific binding of the karyopherin Kap121p to a subunit of the nuclear pore complex containing Nup53p, Nup59p, and Nup170p. J. Cell Biol. 143, 1813–1830 (1998). [PubMed: 9864357]

58. Schrader N, Stelter P, Flemming D, Kunze R, Hurt E, Vetter IR, Structural basis of the nic96 subcomplex organization in the nuclear pore channel. Mol. Cell 29, 46–55 (2008). [PubMed: 18206968]

59. Jeudy S, Schwartz TU, Crystal structure of nucleoporin Nic96 reveals a novel, intricate helical domain architecture. J. Biol. Chem. 282, 34904–34912 (2007). [PubMed: 17897938]

60. Bley CJ, Nie S, Mobbs GW, Petrovic S, Gres AT, Liu X, Mukherjee S, Harvey S, Huber FM, Lin DH, Brown B, Tang AW, Rundlet EJ, Correia AR, Chen S, Regmi SR, Stevens TA, Jette CA, Dasso M, Patke A, Palazzo AF, Kossiakoff AA, Hoelz A, Architechture of the cytoplasmic face of the nuclear pore. Accompanying Manuscript, (2022).

61. Lin DH, Correia AR, Cai SW, Huber FM, Jette CA, Hoelz A, Structural and functional analysis of mRNA export regulation by the nuclear pore complex. Nat. Commun. 9, 2319 (2018). [PubMed: 29899397]

62. Drin G, Casella JF, Gautier R, Boehmer T, Schwartz TU, Antonny B, A general amphipathic alpha-helical motif for sensing membrane curvature. Nat. Struct. Mol. Biol. 14, 138–146 (2007). [PubMed: 17220896]

63. Eisenhardt N, Redolfi J, Antonin W, Interaction of Nup53 with Ndc1 and Nup155 is required for nuclear pore complex assembly. J. Cell Sci. 127, 908–921 (2014). [PubMed: 24363447]

64. Onischenko E, Stanton LH, Madrid AS, Kieselbach T, Weis K, Role of the Ndc1 interaction network in yeast nuclear pore complex assembly and maintenance. J. Cell Biol. 185, 475–491 (2009). [PubMed: 19414609]

65. Ori A, Banterle N, Iskar M, Andres-Pons A, Escher C, Khanh Bui H, Sparks L, Solis-Mezarino V, Rinner O, Bork P, Lemke EA, Beck M, Cell type-specific nuclear pores: a case in point for context-dependent stoichiometry of molecular machines. Mol. Syst. Biol. 9, 648 (2013). [PubMed: 23511206]

66. Griffis ER, Altan N, Lippincott-Schwartz J, Powers MA, Nup98 is a mobile nucleoporin with transcription-dependent dynamics. Mol. Biol. Cell 13, 1282–1297 (2002). [PubMed: 11950939]

67. Rabut G, Doye V, Ellenberg J, Mapping the dynamic organization of the nuclear pore complex inside single living cells. Nat. Cell Biol. 6, 1114–1121 (2004). [PubMed: 15502822]

68. Allen NP, Huang L, Burlingame A, Rexach M, Proteomic analysis of nucleoporin interacting proteins. J. Biol. Chem. 276, 29268–29274 (2001). [PubMed: 11387327]

69. Onischenko E, Tang JH, Andersen KR, Knockenhauer KE, Vallotton P, Derrer CP, Kralt A, Mugler CF, Chan LY, Schwartz TU, Weis K, Natively Unfolded FG Repeats Stabilize the Structure of the Nuclear Pore Complex. Cell 171, 904–917 e919 (2017). [PubMed: 29033133]

70. Levchenko A, Allovalency: a case of molecular entanglement. Curr. Biol. 13, R876–878 (2003). [PubMed: 14614843]

71. Olsen JG, Teilum K, Kragelund BB, Behaviour of intrinsically disordered proteins in protein-protein complexes with an emphasis on fuzziness. Cell. Mol. Life Sci. 74, 3175–3183 (2017). [PubMed: 28597296]

72. Laurell E, Beck K, Krupina K, Theerthagiri G, Bodenmiller B, Horvath P, Aebersold R, Antonin W, Kutay U, Phosphorylation of Nup98 by multiple kinases is crucial for NPC disassembly during mitotic entry. Cell 144, 539–550 (2011). [PubMed: 21335236]

73. Linder MI, Kohler M, Boersema P, Weberruss M, Wandke C, Marino J, Ashiono C, Picotti P, Antonin W, Kutay U, Mitotic Disassembly of Nuclear Pore Complexes Involves CDK1- and PLK1-Mediated Phosphorylation of Key Interconnecting Nucleoporins. Dev. Cell 43, 141–156 e147 (2017). [PubMed: 29065306]

74. Gough SM, Slape CI, Aplan PD, NUP98 gene fusions and hematopoietic malignancies: common themes and new biologic insights. Blood 118, 6247–6257 (2011). [PubMed: 21948299]

75. Regmi SG, Lee H, Kaufhold R, Fichtman B, Chen S, Aksenova V, Turcotte E, Harel A, Arnaoutov A, Dasso M, The Nuclear Pore Complex consists of two independent scaffolds. bioRxiv, 2020.2011.2013.381947 (2020).

76. Braun DA, Sadowski CE, Kohl S, Lovric S, Astrinidis SA, Pabst WL, Gee HY, Ashraf S, Lawson JA, Shril S, Airik M, Tan W, Schapiro D, Rao J, Choi WI, Hermle T, Kemper MJ, Pohl M, Ozaltin F, Konrad M, Bogdanovic R, Buscher R, Helmchen U, Serdaroglu E, Lifton RP, Antonin W, Hildebrandt F, Mutations in nuclear pore genes NUP93, NUP205 and XPO5 cause steroid-resistant nephrotic syndrome. Nat. Genet. 48, 457–465 (2016). [PubMed: 26878725]

77. Muir AM, Cohen JL, Sheppard SE, Guttipatti P, Lo TY, Weed N, Doherty D, DeMarzo D, Fagerberg CR, Kjaersgaard L, Larsen MJ, Rump P, Lohner K, Hirsch Y, Zeevi DA, Zackai EH, Bhoj E, Song Y, Mefford HC, Bi-allelic Loss-of-Function Variants in NUP188 Cause a Recognizable Syndrome Characterized by Neurologic, Ocular, and Cardiac Abnormalities. Am. J. Hum. Genet. 106, 623–631 (2020). [PubMed: 32275884]

78. Ungricht R, Klann M, Horvath P, Kutay U, Diffusion and retention are major determinants of protein targeting to the inner nuclear membrane. J. Cell Biol. 209, 687–703 (2015). [PubMed: 26056139]

79. Ohba T, Schirmer EC, Nishimoto T, Gerace L, Energy- and temperature-dependent transport of integral proteins to the inner nuclear membrane via the nuclear pore. J. Cell Biol. 167, 1051–1062 (2004). [PubMed: 15611332]

80. Zuleger N, Kelly DA, Richardson AC, Kerr AR, Goldberg MW, Goryachev AB, Schirmer EC, System analysis shows distinct mechanisms and common principles of nuclear envelope protein dynamics. J. Cell Biol. 193, 109–123 (2011). [PubMed: 21444689]

81. King MC, Lusk CP, Blobel G, Karyopherin-mediated import of integral inner nuclear membrane proteins. Nature 442, 1003–1007 (2006). [PubMed: 16929305]

82. Meinema AC, Laba JK, Hapsari RA, Otten R, Mulder FA, Kralt A, van den Bogaart G, Lusk CP, Poolman B, Veenhoff LM, Long unfolded linkers facilitate membrane protein import through the nuclear pore complex. Science 333, 90–93 (2011). [PubMed: 21659568]

83. Lokareddy RK, Hapsari RA, van Rheenen M, Pumroy RA, Bhardwaj A, Steen A, Veenhoff LM, Cingolani G, Distinctive Properties of the Nuclear Localization Signals of Inner Nuclear Membrane Proteins Heh1 and Heh2. Structure 23, 1305–1316 (2015). [PubMed: 26051712]

84. Popken P, Ghavami A, Onck PR, Poolman B, Veenhoff LM, Size-dependent leak of soluble and membrane proteins through the yeast nuclear pore complex. Mol. Biol. Cell 26, 1386–1394 (2015). [PubMed: 25631821]

85. Kralt A, Jagalur NB, van den Boom V, Lokareddy RK, Steen A, Cingolani G, Fornerod M, Veenhoff LM, Conservation of inner nuclear membrane targeting sequences in mammalian Pom121 and yeast Heh2 membrane proteins. Mol. Biol. Cell 26, 3301–3312 (2015). [PubMed: 26179916]

86. Zhang Y, Li S, Zeng C, Huang G, Zhu X, Wang Q, Wang K, Zhou Q, Yan C, Zhang W, Yang G, Liu M, Tao Q, Lei J, Shi Y, Molecular architecture of the luminal ring of the Xenopus laevis nuclear pore complex. Cell Res. 30, 532–540 (2020). [PubMed: 32367042]

87. Elosegui-Artola A, Andreu I, Beedle AEM, Lezamiz A, Uroz M, Kosmalska AJ, Oria R, Kechagia JZ, Rico-Lastres P, Le Roux AL, Shanahan CM, Trepat X, Navajas D, Garcia-Manyes S, Roca-Cusachs P, Force Triggers YAP Nuclear Entry by Regulating Transport across Nuclear Pores. Cell 171, 1397–1410 e1314 (2017). [PubMed: 29107331]

88. Frey S, Gorlich D, A saturated FG-repeat hydrogel can reproduce the permeability properties of nuclear pore complexes. Cell 130, 512–523 (2007). [PubMed: 17693259]

89. Petrovic S, Samanta D, Perriches T, Bley CJ, Thierbach K, Brown B, Nie S, Mobbs GW, Stevens TA, Liu X, Tomaleri GP, Schaus L, Hoelz A, Architecture of the linker-scaffold in the nuclear pore, Version 1.0, CaltechDATA (2021). doi: 10.22002/D1.2208.

90. Fontoura BM, Blobel G, Matunis MJ, A conserved biogenesis pathway for nucleoporins: proteolytic processing of a 186-kilodalton precursor generates Nup98 and the novel nucleoporin, Nup96. J. Cell Biol. 144, 1097–1112 (1999). [PubMed: 10087256]

91. Kendirgi F, Rexer DJ, Alcazar-Roman AR, Onishko HM, Wente SR, Interaction between the shuttling mRNA export factor Gle1 and the nucleoporin hCG1: a conserved mechanism in the export of Hsp70 mRNA. Mol. Biol. Cell 16, 4304–4315 (2005). [PubMed: 16000379]

92. Hoelz A, Nairn AC, Kuriyan J, Crystal structure of a tetradecameric assembly of the association domain of Ca2+/calmodulin-dependent kinase II. Mol. Cell 11, 1241–1251 (2003). [PubMed: 12769848]

93. Mossessova E, Lima CD, Ulp1-SUMO crystal structure and genetic analysis reveal conserved interactions and a regulatory element essential for cell growth in yeast. Mol. Cell 5, 865–876 (2000). [PubMed: 10882122]

94. Romier C, Ben Jelloul M, Albeck S, Buchwald G, Busso D, Celie PHN, Christodoulou E, De Marco V, van Gerwen S, Knipscheer P, Lebbink JH, Notenboom V, Poterszman A, Rochel N, Cohen SX, Unger T, Sussman JL, Moras D, Sixma TK, Perrakis A, Co-expression of protein complexes in prokaryotic and eukaryotic hosts: experimental procedures, database tracking and case studies. *Acta Crystallogr.* D Biol. Crystallogr. 62, 1232–1242 (2006). [PubMed: 17001100]

95. Doublie S, Preparation of selenomethionyl proteins for phase determination. Methods Enzymol. 276, 523–530 (1997).

96. Wyatt PJ, Multiangle light scattering: The basic tool for macromolecular characterization. Instrum. Sci. Technol. 25, 1–18 (1997).

97. Kabsch W, Xds. Acta Crystallogr. D Biol. Crystallogr 66, 125–132 (2010). [PubMed: 20124692]

98. Emsley P, Lohkamp B, Scott WG, Cowtan K, Features and development of Coot. *Acta Crystallogr. D* Biol. Crystallogr. 66, 486–501 (2010). [PubMed: 20383002]

99. Liebschner D, Afonine PV, Baker ML, Bunkoczi G, Chen VB, Croll TI, Hintze B, Hung LW, Jain S, McCoy AJ, Moriarty NW, Oeffner RD, Poon BK, Prisant MG, Read RJ, Richardson JS, Richardson DC, Sammito MD, Sobolev OV, Stockwell DH, Terwilliger TC, Urzhumtsev

AG, Videau LL, Williams CJ, Adams PD, Macromolecular structure determination using X-rays, neutrons and electrons: recent developments in Phenix. *Acta Crystallogr. D Struct. Biol*. 75, 861–877 (2019). [PubMed: 31588918]

100. Williams CJ, Headd JJ, Moriarty NW, Prisant MG, Videau LL, Deis LN, Verma V, Keedy DA, Hintze BJ, Chen VB, Jain S, Lewis SM, Arendall WB 3rd, Snoeyink J, Adams PD, Lovell SC, Richardson JS, Richardson DC, MolProbity: More and better reference data for improved all-atom structure validation. Protein Sci. 27, 293–315 (2018). [PubMed: 29067766]
101. Vonrhein C, Blanc E, Roversi P, Bricogne G, Automated structure solution with autoSHARP. Methods Mol. Biol. 364, 215–230 (2007). [PubMed: 17172768]
102. Winter G, Waterman DG, Parkhurst JM, Brewster AS, Gildea RJ, Gerstel M, Fuentes-Montero L, Vollmar M, Michels-Clark T, Young ID, Sauter NK, Evans G, DIALS: implementation and evaluation of a new integration package. Acta Crystallogr. D Struct. Biol. 74, 85–97 (2018). [PubMed: 29533234]
103. Winn MD, Ballard CC, Cowtan KD, Dodson EJ, Emsley P, Evans PR, Keegan RM, Krissinel EB, Leslie AG, McCoy A, McNicholas SJ, Murshudov GN, Pannu NS, Potterton EA, Powell HR, Read RJ, Vagin A, Wilson KS, Overview of the CCP4 suite and current developments. *Acta* Crystallogr. D Biol. Crystallogr. 67, 235–242 (2011). [PubMed: 21460441]
104. Painter J, Merritt EA, Optimal description of a protein structure in terms of multiple groups undergoing TLS motion. *Acta* Crystallogr. D Biol. Crystallogr. 62, 439–450 (2006). [PubMed: 16552146]
105. McCoy AJ, Grosse-Kunstleve RW, Adams PD, Winn MD, Storoni LC, Read RJ, Phaser crystallographic software. J. Appl. Crystallogr. 40, 658–674 (2007). [PubMed: 19461840]
106. Tiwari SP, Fuglebakk E, Hollup SM, Skjaerven L, Cragnolini T, Grindhaug SH, Tekle KM, Reuter N, WEBnm@ v2.0: Web server and services for comparing protein flexibility. BMC Bioinformatics 15, 427 (2014). [PubMed: 25547242]
107. Terwilliger TC, Grosse-Kunstleve RW, Afonine PV, Moriarty NW, Zwart PH, Hung LW, Read RJ, Adams PD, Iterative model building, structure refinement and density modification with the PHENIX AutoBuild wizard. *Acta Crystallogr. D* Biol. Crystallogr. 64, 61–69 (2008). [PubMed: 18094468]
108. Wang JW, Chen JR, Gu YX, Zheng CD, Jiang F, Fan HF, Terwilliger TC, Hao Q, SAD phasing by combination of direct methods with the SOLVE/RESOLVE procedure. *Acta Crystallogr.* D Biol. Crystallogr. 60, 1244–1253 (2004). [PubMed: 15213386]
109. Terwilliger T, SOLVE and RESOLVE: automated structure solution, density modification and model building. J. Synchrotron Radiat 11, 49–52 (2004). [PubMed: 14646132]
110. Mastronarde DN, Automated electron microscope tomography using robust prediction of specimen movements. J. Struct. Biol. 152, 36–51 (2005). [PubMed: 16182563]
111. Thompson RF, Iadanza MG, Hesketh EL, Rawson S, Ranson NA, Collection, pre-processing and on-the-fly analysis of data for high-resolution, single-particle cryo-electron microscopy. Nat. Protoc. 14, 100–118 (2019). [PubMed: 30487656]
112. Zheng SQ, Palovcak E, Armache JP, Verba KA, Cheng Y, Agard DA, MotionCor2: anisotropic correction of beam-induced motion for improved cryo-electron microscopy. Nat. Methods 14, 331–332 (2017). [PubMed: 28250466]
113. Punjani A, Rubinstein JL, Fleet DJ, Brubaker MA, cryoSPARC: algorithms for rapid unsupervised cryo-EM structure determination. Nat. Methods 14, 290–296 (2017). [PubMed: 28165473]
114. Zivanov J, Nakane T, Forsberg BO, Kimanius D, Hagen WJ, Lindahl E, Scheres SH, New tools for automated high-resolution cryo-EM structure determination in RELION-3. Elife 7, e4216 (2018).
115. Scheres SH, RELION: implementation of a Bayesian approach to cryo-EM structure determination. J. Struct. Biol. 180, 519–530 (2012). [PubMed: 23000701]
116. Tan YZ, Baldwin PR, Davis JH, Williamson JR, Potter CS, Carragher B, Lyumkis D, Addressing preferred specimen orientation in single-particle cryo-EM through tilting. Nat. Methods 14, 793–796 (2017). [PubMed: 28671674]
117. Asarnow D, Palovcak E, Cheng Y, asarnow/pyem: UCSF pyem v0.5, (2019).

118. Pettersen EF, Goddard TD, Huang CC, Couch GS, Greenblatt DM, Meng EC, Ferrin TE, UCSF Chimera--a visualization system for exploratory research and analysis. J. Comput. Chem. 25, 1605–1612 (2004). [PubMed: 15264254]

119. Afonine PV, Poon BK, Read RJ, Sobolev OV, Terwilliger TC, Urzhumtsev A, Adams PD, Real-space refinement in PHENIX for cryo-EM and crystallography. Acta Crystallogr. D Struct. Biol. 74, 531–544 (2018). [PubMed: 29872004]

120. Barad BA, Echols N, Wang RY, Cheng Y, DiMaio F, Adams PD, Fraser JS, EMRinger: side chain-directed model and map validation for 3D cryo-electron microscopy. Nat. Methods 12, 943–946 (2015). [PubMed: 26280328]

121. Punjani A, Zhang H, Fleet DJ, Non-uniform refinement: adaptive regularization improves single-particle cryo-EM reconstruction. Nat. Methods 17, 1214–1221 (2020). [PubMed: 33257830]

122. Terwilliger TC, Sobolev OV, Afonine PV, Adams PD, Automated map sharpening by maximization of detail and connectivity. Acta Crystallogr. D Struct. Biol. 74, 545–559 (2018). [PubMed: 29872005]

123. Jakobi AJ, Wilmanns M, Sachse C, Model-based local density sharpening of cryo-EM maps. Elife 6, e27131 (2017). [PubMed: 29058676]

124. Pei J, Kim BH, Grishin NV, PROMALS3D: a tool for multiple protein sequence and structure alignments. Nucleic Acids Res. 36, 2295–2300 (2008). [PubMed: 18287115]

125. Katoh K, Standley DM, MAFFT multiple sequence alignment software version 7: improvements in performance and usability. Mol. Biol. Evol. 30, 772–780 (2013). [PubMed: 23329690]

126. Barton GJ, ALSCRIPT: a tool to format multiple sequence alignments. Protein Eng. 6, 37–40 (1993). [PubMed: 8433969]

127. Sikorski RS, Hieter P, A system of shuttle vectors and yeast host strains designed for efficient manipulation of DNA in Saccharomyces cerevisiae. Genetics 122, 19–27 (1989). [PubMed: 2659436]

128. Janke C, Magiera MM, Rathfelder N, Taxis C, Reber S, Maekawa H, Moreno-Borchart A, Doenges G, Schwob E, Schiebel E, Knop M, A versatile toolbox for PCR-based tagging of yeast genes: new fluorescent proteins, more markers and promoter substitution cassettes. Yeast 21, 947–962 (2004). [PubMed: 15334558]

129. Longtine MS, McKenzie A 3rd, Demarini DJ, Shah NG, Wach A, Brachat A, Philippsen P, Pringle JR, Additional modules for versatile and economical PCR-based gene deletion and modification in Saccharomyces cerevisiae. Yeast 14, 953–961 (1998). [PubMed: 9717241]

130. Wadia JS, Stan RV, Dowdy SF, Transducible TAT-HA fusogenic peptide enhances escape of TAT-fusion proteins after lipid raft macropinocytosis. Nat. Med. 10, 310–315 (2004). [PubMed: 14770178]

131. Yaffe MP, Schatz G, Two nuclear mutations that block mitochondrial protein import in yeast. Proc. Natl. Acad. Sci. U.S.A. 81, 4819–4823 (1984). [PubMed: 6235522]

132. Gwizdek C, Iglesias N, Rodriguez MS, Ossareh-Nazari B, Hobeika M, Divita G, Stutz F, Dargemont C, Ubiquitin-associated domain of Mex67 synchronizes recruitment of the mRNA export machinery with transcription. Proc. Natl. Acad. Sci. U.S.A. 103, 16376–16381 (2006). [PubMed: 17056718]

133. Huang G, Zhang Y, Zhu X, Zeng C, Wang Q, Zhou Q, Tao Q, Liu M, Lei J, Yan C, Shi Y, Structure of the cytoplasmic ring of the Xenopus laevis nuclear pore complex by cryo-electron microscopy single particle analysis. Cell Res. 30, 520–531 (2020). [PubMed: 32376910]

134. Flory PJ, Volkenstein M, Statistical mechanics of chain molecules. Biopolymers 8, 699–700 (1969).

135. Evers TH, van Dongen EM, Faesen AC, Meijer EW, Merkx M, Quantitative understanding of the energy transfer between fluorescent proteins connected via flexible peptide linkers. Biochemistry 45, 13183–13192 (2006). [PubMed: 17073440]

136. Waskom ML, seaborn:statistical data visualization. J. Open Source Sotfw 6, (2021).

137. Stuwe T, von Borzyskowski LS, Davenport AM, Hoelz A, Molecular basis for the anchoring of proto-oncoprotein Nup98 to the cytoplasmic face of the nuclear pore complex. J. Mol. Biol. 419, 330–346 (2012). [PubMed: 22480613]

138. Ho AK, Shen TX, Ryan KJ, Kiseleva E, Levy MA, Allen TD, Wente SR, Assembly and preferential localization of Nup116p on the cytoplasmic face of the nuclear pore complex by interaction with Nup82p. Mol. Cell. Biol. 20, 5736–5748 (2000). [PubMed: 10891509]

139. Teixeira MT, Siniossoglou S, Podtelejnikov S, Benichou JC, Mann M, Dujon B, Hurt E, Fabre E, Two functionally distinct domains generated by in vivo cleavage of Nup145p: a novel biogenesis pathway for nucleoporins. EMBO J. 16, 5086–5097 (1997). [PubMed: 9305650]

140. Wente SR, Blobel G, NUP145 encodes a novel yeast glycine-leucine-phenylalanine-glycine (GLFG) nucleoporin required for nuclear envelope structure. J. Cell Biol. 125, 955–969 (1994). [PubMed: 8195299]

141. Rajoo S, Vallotton P, Onischenko E, Weis K, Stoichiometry and compositional plasticity of the yeast nuclear pore complex revealed by quantitative fluorescence microscopy. Proc. Natl. Acad. Sci. U.S.A. 115, E3969–E3977 (2018). [PubMed: 29632211]

142. Rout MP, Aitchison JD, Suprapto A, Hjertaas K, Zhao Y, Chait BT, The yeast nuclear pore complex: composition, architecture, and transport mechanism. J. Cell Biol. 148, 635–651 (2000). [PubMed: 10684247]

143. Lusk CP, Makhnevych T, Marelli M, Aitchison JD, Wozniak RW, Karyopherins in nuclear pore biogenesis: a role for Kap121p in the assembly of Nup53p into nuclear pore complexes. J. Cell Biol. 159, 267–278 (2002). [PubMed: 12403813]

144. Schindelin J, Arganda-Carreras I, Frise E, Kaynig V, Longair M, Pietzsch T, Preibisch S, Rueden C, Saalfeld S, Schmid B, Tinevez JY, White DJ, Hartenstein V, Eliceiri K, Tomancak P, Cardona A, Fiji: an open-source platform for biological-image analysis. Nat. Methods 9, 676–682 (2012). [PubMed: 22743772]

145. Jeanmougin F, Thompson JD, Gouy M, Higgins DG, Gibson TJ, Multiple sequence alignment with Clustal X. Trends Biochem. Sci 23, 403–405 (1998). [PubMed: 9810230]

146. Christianson TW, Sikorski RS, Dante M, Shero JH, Hieter P, Multifunctional yeast high-copy-number shuttle vectors. Gene 110, 119–122 (1992). [PubMed: 1544568]

147. Fernandez-Martinez J, Kim SJ, Shi Y, Upla P, Pellarin R, Gagnon M, Chemmama IE, Wang J, Nudelman I, Zhang W, Williams R, Rice WJ, Stokes DL, Zenklusen D, Chait BT, Sali A, Rout MP, Structure and Function of the Nuclear Pore Complex Cytoplasmic mRNA Export Platform. Cell 167, 1215–1228 e1225 (2016). [PubMed: 27839866]

148. Romes EM, Tripathy A, Slep KC, Structure of a yeast Dyn2-Nup159 complex and molecular basis for dynein light chain-nuclear pore interaction. J Biol Chem 287, 15862–15873 (2012). [PubMed: 22411995]

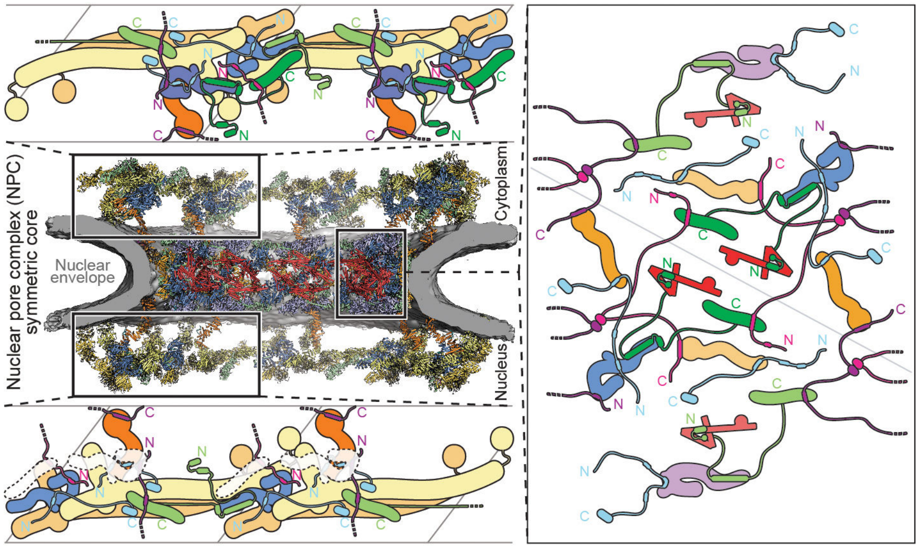

Fig. 0. Linker-scaffold architecture in the human NPC's symmetric core.

Near-atomic composite structure of the NPC symmetric core obtained by quantitative docking of high-resolution crystal and single particle cryo-EM structures into a cryo-ET reconstruction of the intact human NPC. Schematic representations of the intricate linker-scaffold topology of the cytoplasmic outer ring, inner ring, and nuclear outer ring (clockwise), depicted for the boxed regions.

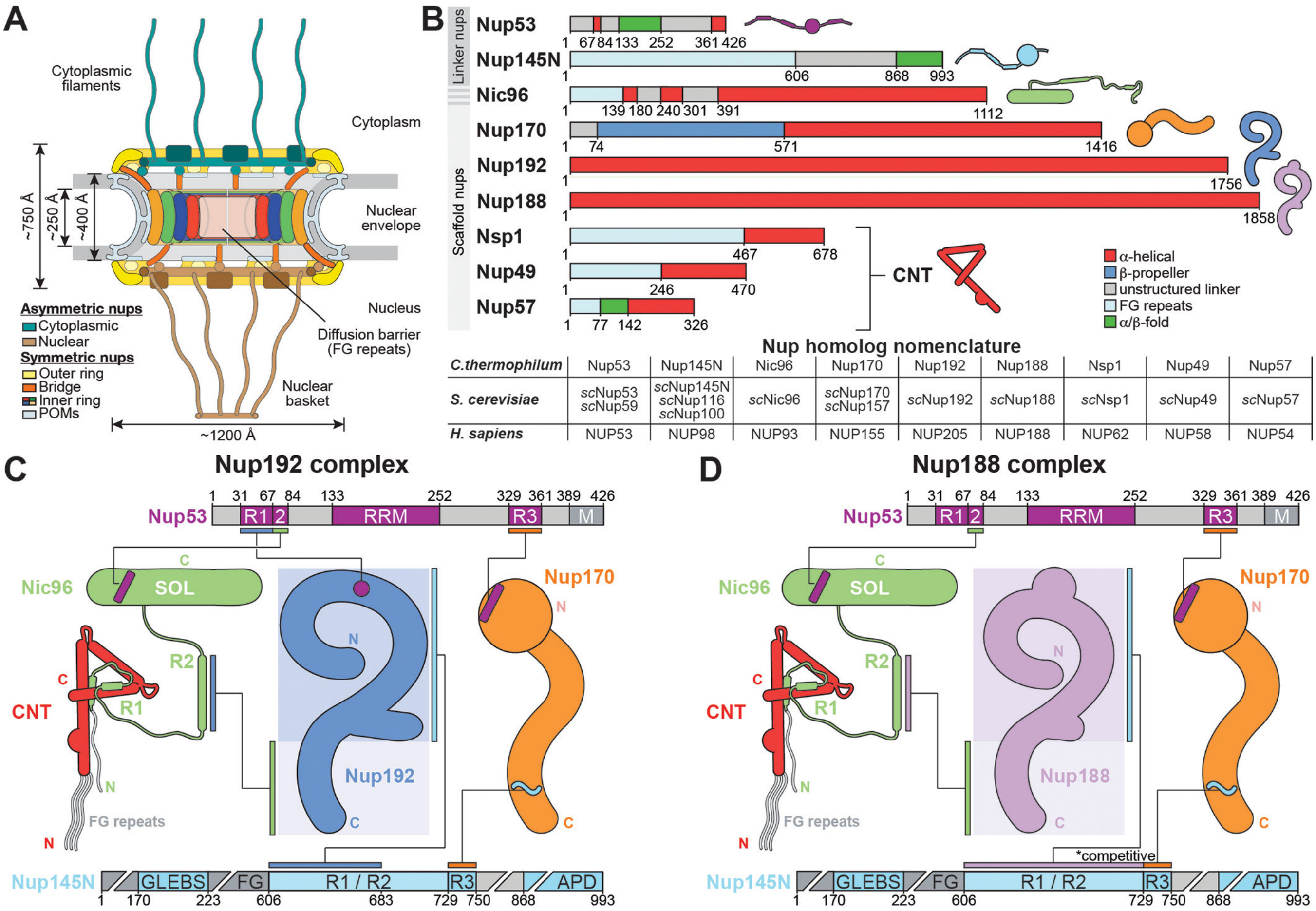

C.thermophilum	Nup53	Nup145N	Nic96	Nup170	Nup192	Nup188	Nsp1	Nup49	Nup57
S. cerevisiae	*sc*Nup53 *sc*Nup59	*sc*Nup145N *sc*Nup116 *sc*Nup100	*sc*Nic96	*sc*Nup170 *sc*Nup157	*sc*Nup192	*sc*Nup188	*sc*Nsp1	*sc*Nup49	*sc*Nup57
H. sapiens	NUP53	NUP98	NUP93	NUP155	NUP205	NUP188	NUP62	NUP58	NUP54

Fig. 1. Outline of the symmetric core inner ring architecture.

(**A**) Cross-sectional schematic of the NPC architecture. (**B**) Domain structures of the *Chaetomium thermophilum* inner ring linker and scaffold nucleoporins (nups). Nic96 consists of linker (residues 1–390) and scaffold (residues 391–1112) regions. Nomenclature for nup homologs from *C.thermophilum, Saccharomyces cerevisiae, and Homo sapiens*. Multiple paralogs exist for some *S.cerevisiae* nups. (**C**, **D**) Schematic map of previously established linker-scaffold interactions in alternative, mutually exclusive inner ring complexes organized around Nup192 and Nup188 scaffold hubs (35). Black lines connecting colored bars indicate interactions between nup regions.

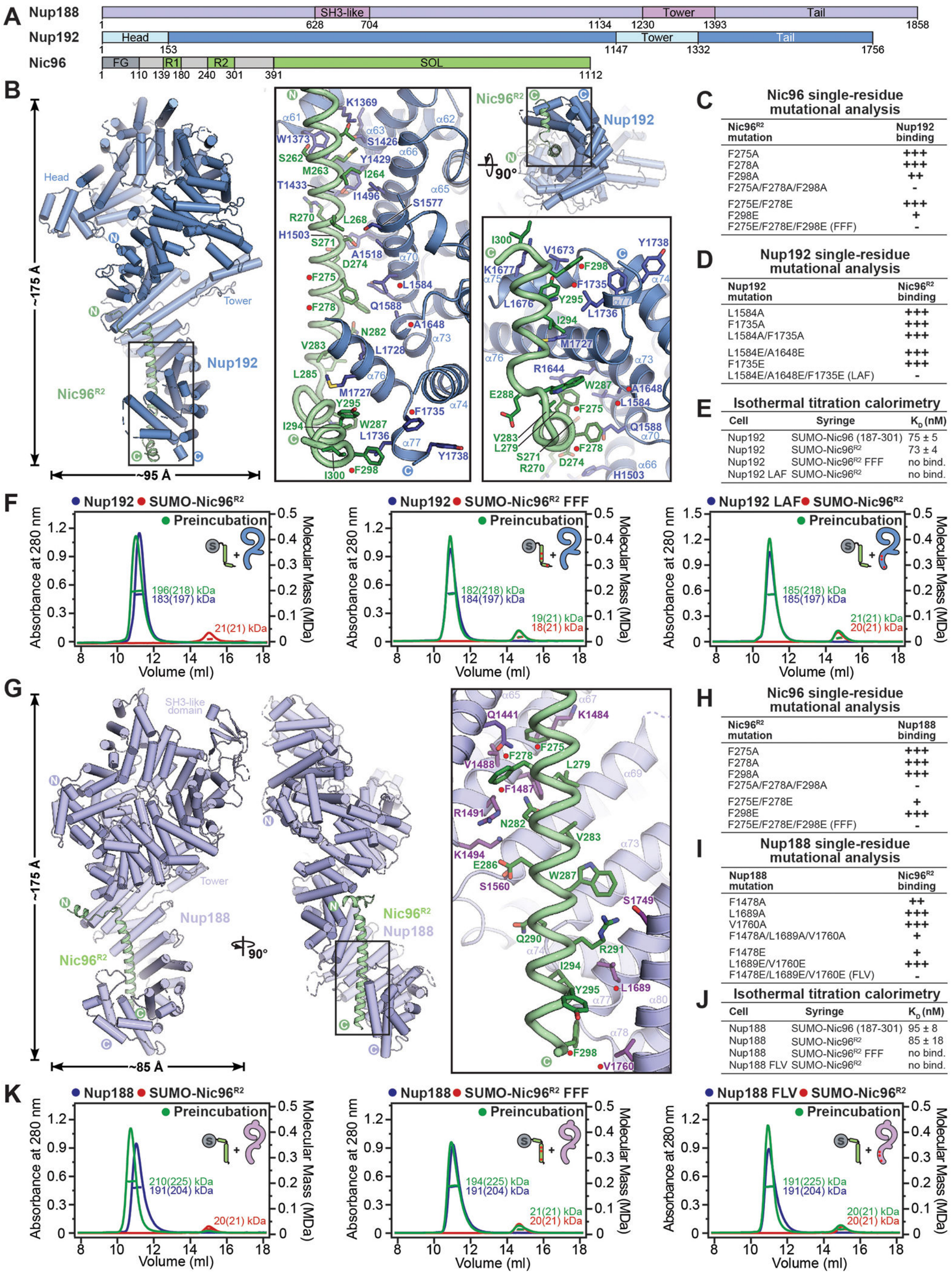

C Nic96 single-residue mutational analysis

Nic96^{R2} mutation	Nup192 binding
F275A	+++
F278A	+++
F298A	++
F275A/F278A/F298A	-
F275E/F278E	+++
F298E	+
F275E/F278E/F298E (FFF)	-

D Nup192 single-residue mutational analysis

Nup192 mutation	Nic96^{R2} binding
L1584A	+++
F1735A	+++
L1584A/F1735A	+++
L1584E/A1648E	+++
F1735E	+++
L1584E/A1648E/F1735E (LAF)	-

E Isothermal titration calorimetry

Cell	Syringe	K_D (nM)
Nup192	SUMO-Nic96 (187-301)	75 ± 5
Nup192	SUMO-Nic96^{R2}	73 ± 4
Nup192	SUMO-Nic96^{R2} FFF	no bind.
Nup192 LAF	SUMO-Nic96^{R2}	no bind.

H Nic96 single-residue mutational analysis

Nic96^{R2} mutation	Nup188 binding
F275A	+++
F278A	+++
F298A	+++
F275A/F278A/F298A	-
F275E/F278E	+
F298E	+++
F275E/F278E/F298E (FFF)	-

I Nup188 single-residue mutational analysis

Nup188 mutation	Nic96^{R2} binding
F1478A	++
L1689A	+++
V1760A	+++
F1478A/L1689A/V1760A	+
F1478E	+
L1689E/V1760E	+++
F1478E/L1689E/V1760E (FLV)	-

J Isothermal titration calorimetry

Cell	Syringe	K_D (nM)
Nup188	SUMO-Nic96 (187-301)	95 ± 8
Nup188	SUMO-Nic96^{R2}	85 ± 18
Nup188	SUMO-Nic96^{R2} FFF	no bind.
Nup188 FLV	SUMO-Nic96^{R2}	no bind.

Fig. 2. Structural and biochemical analyses of the Nup192-Nic96 and Nup188-Nic96 interactions. (**A**) Domain structures of *C.thermophilum* Nup188, Nup192, and Nic96. (**B**) Cartoon representation of the 3.8Å *C.thermophilum* Nup192•Nic96^{R2} single particle cryo-EM structure. Inset regions are magnified to illustrate the molecular details of the Nup192-Nic96 interaction. Red circles indicate residues involved in the Nup192-Nic96 interaction. (**C**, **D**) Summary of structure-guided (C) SUMO-Nic96^{R2} and (D) Nup192 mutations' effect on Nup192•SUMO-Nic96^{R2} complex formation, assayed by size-exclusion chromatography (SEC); (+++) no effect, (++) weak effect, (+) moderate effect, (−) abolished binding.

(**E**) Dissociation constants (K_Ds) determined by triplicate isothermal titration calorimetry (ITC) experiments, with the mean and associated standard error reported. (**F**) SEC coupled to multi-angle light scattering (SEC-MALS) interaction analyses of Nup192•SUMO-Nic96^{R2} and interaction-abolishing mutants. Measured molecular masses are indicated, with theoretical masses in parentheses. (**G**) Two views in cartoon representation of the 4.4Å *C.thermophilum* Nup188•Nic96^{R2} crystal structure phased and built with the 2.8Å Nup188^{NTD} and 3.4Å Nup188^{Tail} (PDB ID 5CWU) (28) crystal structures. Inset regions are magnified to illustrate the molecular details of the Nup188-Nic96^{R2} interaction. Red circles indicate residues involved in Nup188-Nic96^{R2} binding. (**H**, **I**) Summary of structure-guided (H) SUMO-Nic96^{R2} and (I) Nup188 mutations' effect on Nup188•SUMO-Nic96^{R2} complex formation, assayed by SEC. (**J**) K_Ds determined by triplicate ITC experiments with the mean and associated standard error reported. (**K**) SEC-MALS analysis of Nup188•SUMO-Nic96^{R2} and interaction-abolishing mutants.

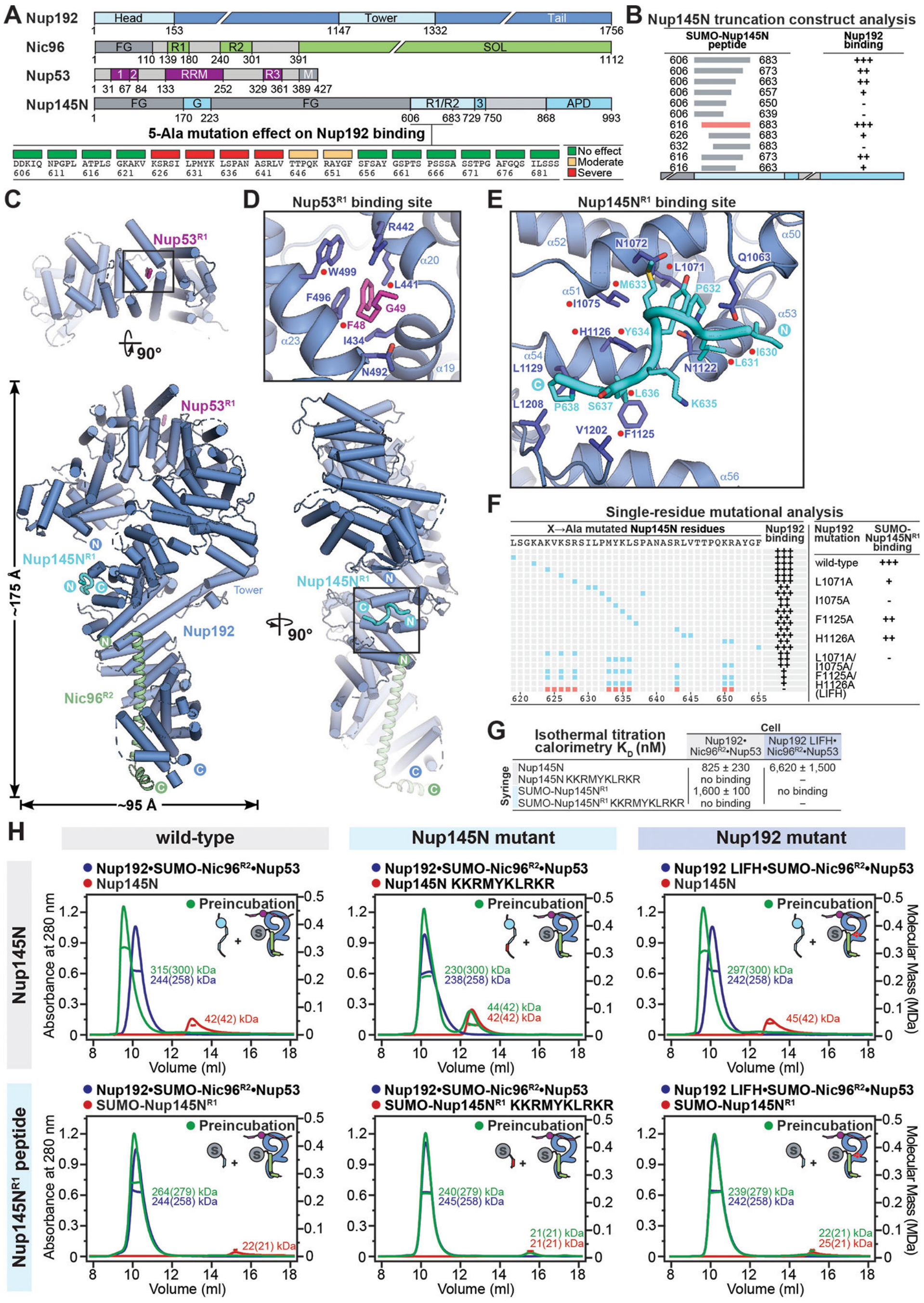

Fig. 3. Structural and biochemical analyses of the Nup192-Nup145N interaction.

(**A**) Domain structures of *C.thermophilum* Nup192, Nic96, Nup53 and Nup145N; effect of each 5-Ala substitution on Nup145N binding to Nup192, assessed by SEC, indicated by colored boxes above Nup145N primary sequence. (**B**) Summary of SEC binding analysis identifying the minimal Nup145N^{R1} (red) region sufficient for Nup192 binding; (+++) no effect, (++) weak effect, (+) moderate effect, and (−) abolished binding. (**C**) Cartoon representation of the 3.2Å *C.thermophilum* Nup192•Nic96^{R2}•Nup53^{R1}•Nup145N^{R1} single particle cryo-EM structure. Insets indicate regions magnified to illustrate molecular details of (**D**) the Nup192-Nup53^{R1} and (**E**) the Nup192-Nup145N^{R1} interactions. Red circles indicate residues involved in the Nup192-Nup53^{R1} (41) and Nup192-Nup145N^{R1} interactions. (**F**) Effect of Nup145N alanine substitutions (cyan squares) on Nup192 binding, assayed by SEC (*left*). Effect of structure-guided Nup192 alanine substitutions on SUMO-Nup145N^{R1} binding, assayed by SEC (*right*). (**G**) K_Ds determined by triplicate ITC experiments, with the mean and associated standard error reported. (**H**) SEC-MALS analysis of Nup192•SUMO-Nic96^{R2}•Nup53•Nup145N and Nup192•SUMO-Nic96^{R2}•Nup53•SUMO-Nup145N^{R1} complex formation and disruption by mutants. Measured molecular masses are indicated, with respective theoretical masses provided in parentheses.

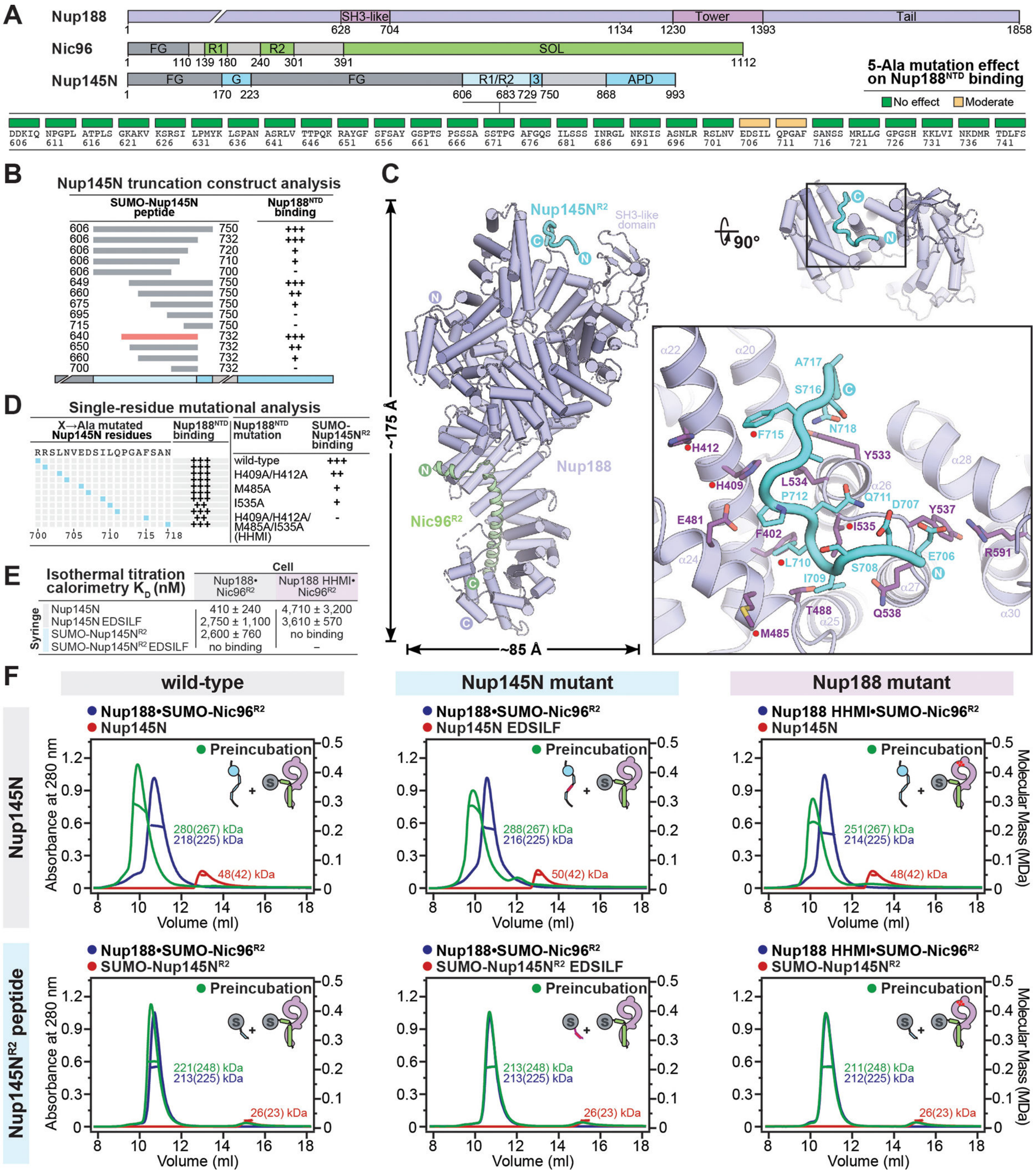

Fig. 4. Structural and biochemical analyses of the Nup188-Nup145N interaction.

(**A**) Domain structures of *C.thermophilum* Nup188, Nic96, and Nup145N; effect of each 5-Ala substitution on Nup145N binding to Nup188^{NTD}, assessed by SEC, indicated by colored boxes above Nup145N primary sequence. (**B**) Summary of SEC binding analysis identifying the minimal Nup145N^{R2} (red) region sufficient for binding to Nup188^{NTD}; (+++) no effect, (++) weak effect, (+) moderate effect, and (−) abolished binding. (**C**) Cartoon representation of the 2.8Å *C.thermophilum* Nup188•Nic96^{R2}•Nup145N^{R2} single particle cryo-EM structure. Inset indicates region magnified to illustrate molecular details of the Nup188-Nup145N^{R2} interaction. Red circles indicate residues involved in the Nup188-Nup145N^{R2} interaction. (**D**) Effect of Nup145N alanine substitutions (cyan squares) on Nup188^{NTD} binding, assayed by SEC (*left*). Effect of structure-guided Nup188^{NTD} alanine substitutions on SUMO-Nup145N^{R2} binding, assayed by SEC (*right*). (**E**) K_Ds determined by triplicate ITC experiments, with the mean and associated standard error reported. (**F**) SEC-MALS analysis of Nup188•SUMO-Nic96^{R2}•Nup145N and Nup188•SUMO-Nic96^{R2}•SUMO-Nup145N^{R2} complex formation and disruption by mutants. Measured molecular masses are indicated, with respective theoretical masses provided in parentheses.

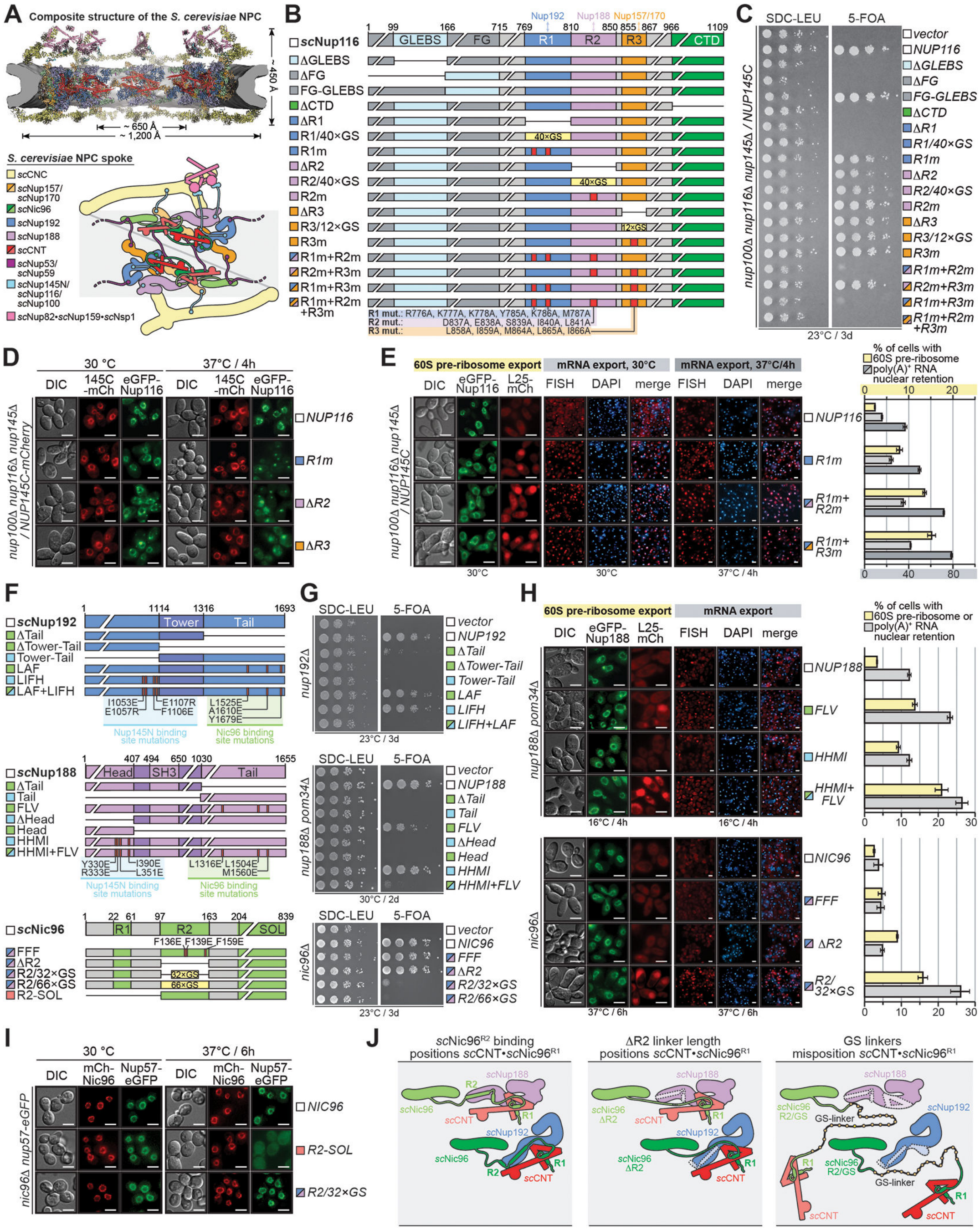

Fig. 5. Functional *in vivo* dissection of the *S.cerevisiae* NPC linker-scaffold.

(**A**) Cross-sectional view of the *S.cerevisiae* NPC composite structure generated by docking linker-scaffold structures into an ~25Å *in situ* sub-tomogram averaged cryo-ET map (EMD-10198) (36) (*top*). Schematic representation of a *S.cerevisiae* NPC spoke (*bottom*). (**B**) Domain structure of *sc*Nup116 variants; Gle2-binding sequence (GLEBS); phenylalanine-glycine repeats (FG); *sc*Nup192-binding region (R1); *sc*Nup188-binding region (R2); *sc*Nup157/170-binding region (R3). (**C**) Viability analysis of a ten-fold dilution series of a *nup100Δnup116Δnup145Δ/NUP145C* strain expressing *sc*Nup116 variants and subjected to 5-FOA selection for loss of rescuing wildtype plasmid. (**D**) Subcellular localization at permissive (30°C) and growth-challenging (37°C) temperatures of a representative subset of eGFP-*sc*Nup116 variants in a *nup100*Δ*nup116*Δ*nup145*Δ/*NUP145C-mCherry* strain. (**E**) Representative images and quantitation (n>500) of subcellular localization of 60S pre-ribosomal export reporter *sc*Rpl25-mCherry and poly(A)$^+$ RNA at 30°C and 37°C, in the presence of a representative subset of *sc*Nup116 variants. (**F**) Domain structures of *sc*Nup192, *sc*Nup188, and *sc*Nic96 variants. (**G**) Viability analysis of a ten-fold dilution series of *nup192*Δ, *nup188*Δ*pom34*Δ, and *nic96*Δ *S.cerevisiae* strains expressing *sc*Nup192, *sc*Nup188, and *sc*Nic96 variants, respectively, and subjected to 5-FOA selection for loss of rescuing wildtype plasmids. (**H**) Representative images and quantitation (n>500) of the nuclear *sc*Rpl25-mCherry and poly(A)$^+$ RNA retention in the presence of *sc*Nup188 and *sc*Nic96 variants at indicated growth-challenging temperatures in *nup188*Δ*pom34*Δ and *nic96*Δ *S.cerevisiae* strains, respectively. (**I**) Subcellular localization at permissive (30°C) and growth-challenging (37°C) temperatures of the *sc*CNT subunit *sc*Nup57-eGFP in the presence of mCherry-*sc*Nic96 variants. (**J**) Schematic model of CNT positioning in wildtype, *sc*Nic96^{R2} deletion, and glycine-serine (GS)-linker replacement strains. Squares associated with variant labels are color-coded according to the nup binding partners targeted by the mutation. All experiments were performed in triplicate. Mean and associated standard error are reported for all quantitation. Scalebars are 5 µm.

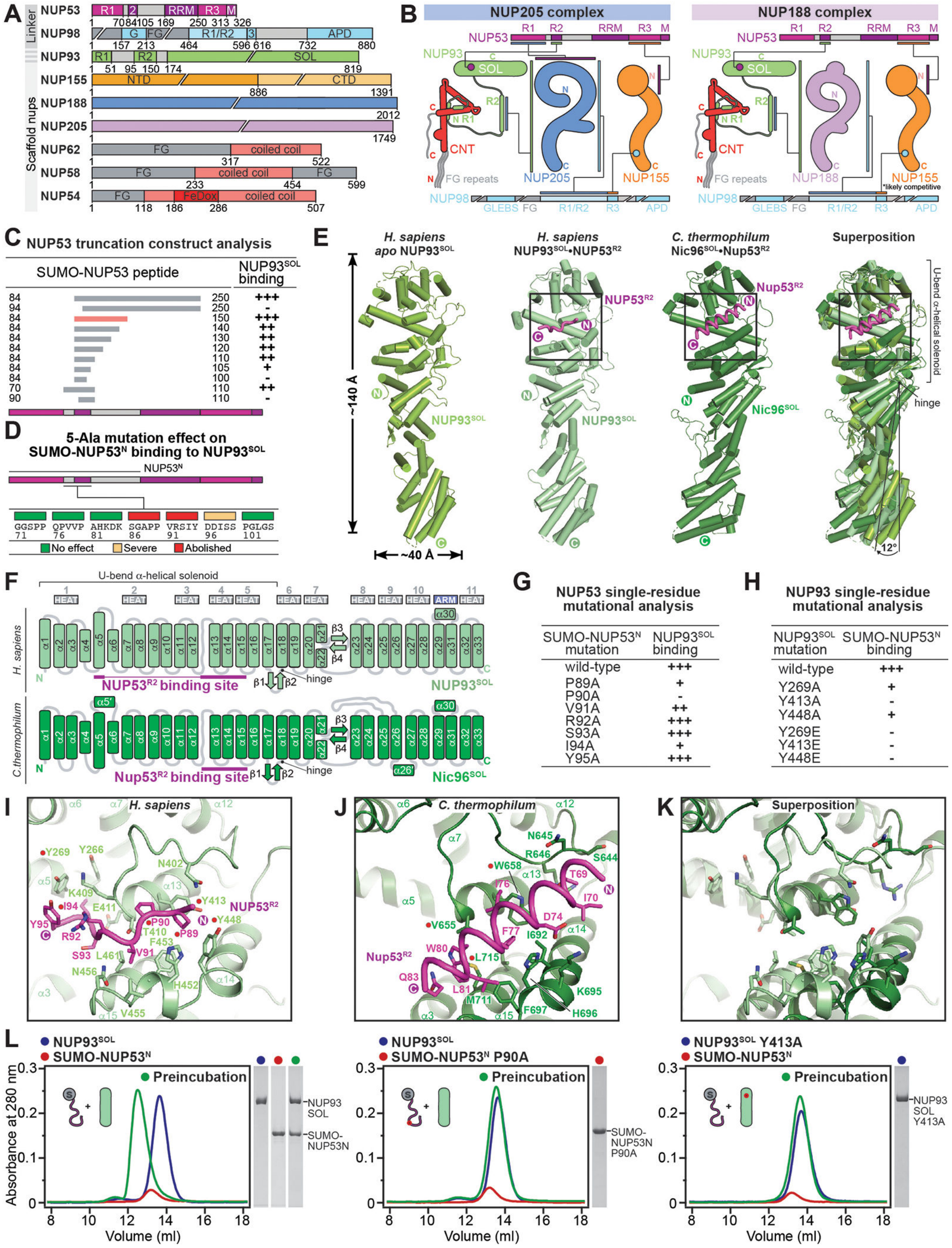

Fig. 6. Evolutionary conservation of the human linker-scaffold network.

(**A**) Domain structures of the human inner ring nups. NUP93 consists of linker (residues 1–173) and scaffold (residues 174–819) regions. (**B**) Schematic summary of the linker-scaffold interactions in complexes organized around the NUP188 and NUP205 scaffold hubs. Black lines connecting colored bars indicate interactions between nup regions. (**C**) Summary of SEC binding analysis identifying the minimal NUP53^{R2} region (red) sufficient for NUP93^{SOL} binding; (+++) no effect, (++) weak effect, (+) moderate effect, and (−) abolished binding. (**D**) Effect of each 5-Ala substitution on SUMO-NUP53^{N}

binding to NUP93^{SOL}, assessed by SEC, indicated by colored boxes above NUP53 primary sequence. (**E**) Cartoon representations of the 2.0Å *H.sapiens apo* NUP93^{SOL}, 3.4Å *H.sapiens* NUP93^{SOL}•NUP53^{R2}, 2.7Å *C.thermophilum* Nic96^{SOL}•Nup53^{R2} (PDB ID 5HB3) (35) crystal structures and their superposition. An ~12° displacement of the C-terminal α-helical solenoid, pivoted about the hinge loop, is observed between the *apo* NUP93^{SOL} and NUP93^{SOL}•NUP53^{R2} structures. (**F**) Schematic of the human NUP93^{SOL} and *C.thermophilum* Nic96^{SOL} fold architectures. (**G**, **H**) Summary of the effect of structure-guided mutations in (G) SUMO-NUP53^{N} and (H) NUP93^{SOL} on NUP93^{SOL}•SUMO-NUP53^{N} complex formation, assayed by SEC. (**I-K**) Magnified views of regions indicated with insets in (E), comparing molecular details of NUP53^{R2}/Nup53^{R2} binding sites. (**L**) SEC analyses of NUP93^{SOL}•SUMO-NUP53^{N} complex formation and disruption by mutants. SDS-PAGE gel strips of peak fractions visualized by Coomassie staining.

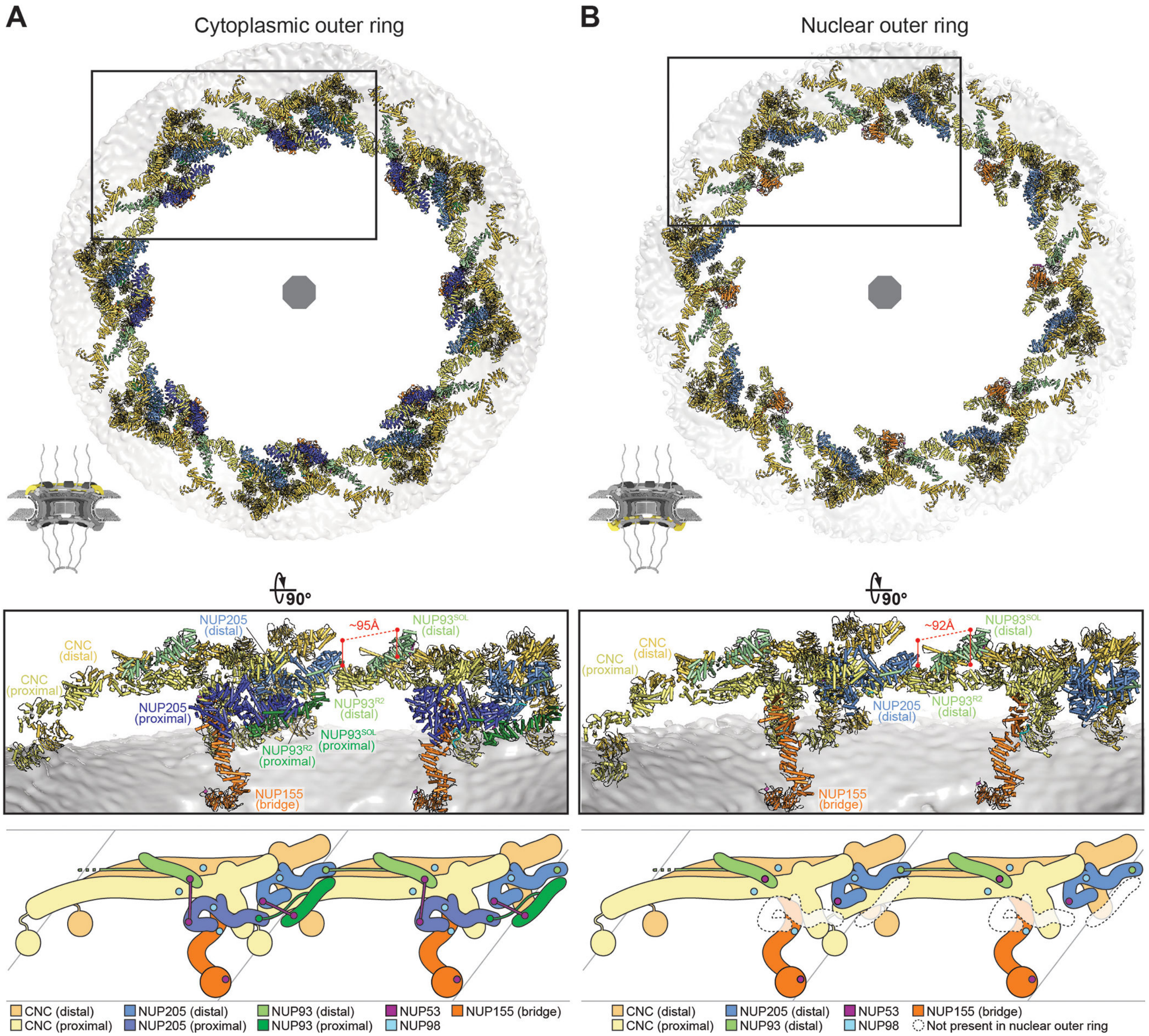

Fig. 7. Architecture of the human NPC symmetric core outer rings.

Composite structure generated by quantitatively docking crystal and single particle cryo-EM structures into an ~12Å cryo-ET map of the intact human NPC (EMD-14322) (47), viewed from the (**A**) cytoplasmic and (**B**) nuclear face. Nuclear envelope and docked structures are rendered in isosurface and cartoon representation, respectively. Insets indicate regions encompassing two spokes (*top*), 90°-rotated and magnified (*middle*), and schematized (*bottom*). Cross-spoke distances between the distal NUP205-bound NUP93^{R2} and distal NUP93^{SOL} are indicated in red. Linker binding sites on scaffold nup surfaces are indicated by colored circles. Dashed transparent shapes indicate the absence of proximal NUP205 and NUP93 from the nuclear outer ring.

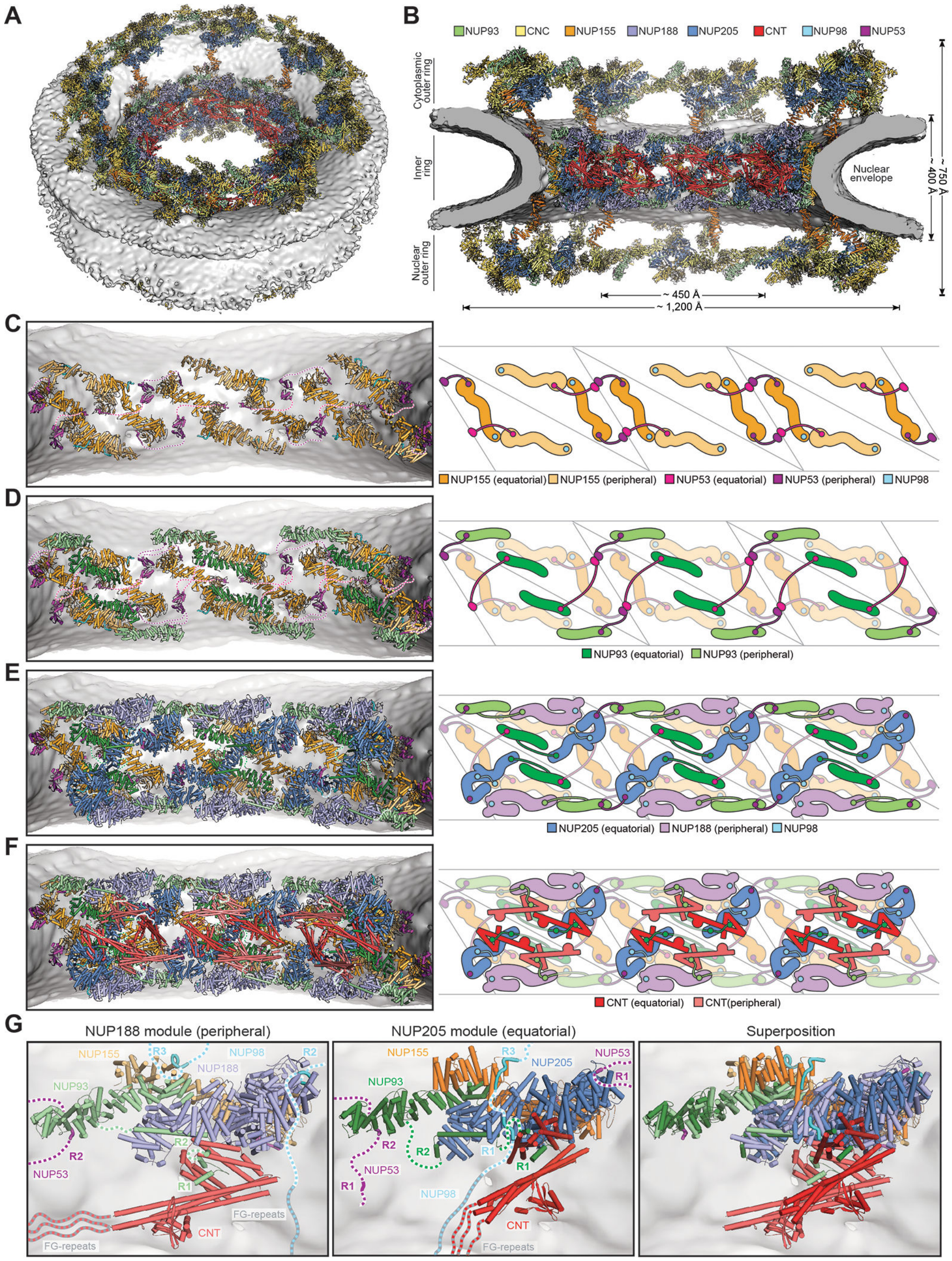

Fig. 8. Linker-scaffold architecture of the human NPC inner ring.

Composite structure generated by quantitatively docking crystal and single particle cryo-EM structures into an ~12Å cryo-ET map of the intact human NPC (EMD-14322) (47), viewed from (**A**) the cytoplasmic face, and (**B**) the central transport channel cross-section. Nuclear envelope and docked structures are rendered in isosurface and cartoon representation, respectively. (**C-F**) Starting from the nuclear envelope, successive layers reveal the architecture of three inner ring spokes of the human NPC. Corresponding schematics illustrate linker paths between binding sites on scaffold surfaces (colored circles). (C)

NUP53^{RRM} domains homodimerize between spokes to link cytoplasmic peripheral with nuclear equatorial, and conversely cytoplasmic equatorial with nuclear peripheral copies of NUP155. (D) NUP53^{RRM} domains link cytoplasmic peripheral with nuclear equatorial, and conversely cytoplasmic equatorial with nuclear peripheral copies of NUP93^{SOL}. (E) NUP205 and NUP188 bind to the equatorial and peripheral NUP93^{R2}, respectively. NUP98 connects NUP205 and equatorial NUP155. NUP53 connects NUP205 and cross-spoke peripheral NUP93^{SOL} (F) CNT is recruited by NUP93^{R1} and positioned by NUP93^{R2} binding to NUP188 and NUP205. (**G**) Closeup views of inner ring modules assembled around NUP188 and NUP205 scaffold hubs, and their superposition. Dashed lines indicate unstructured linker nup segments and FG-repeat regions.

Movie 1. Structural analysis of the Nup192 and Nup188 inner ring complexes.

Comparison of crystal and single-particle cryo-EM structures of *C. thermophilum* Nup192 and Nup188 scaffolds in complex with Nic96, Nup145N, and Nup53 linkers. Cryo-EM densities are rendered as isosurfaces colored according to their assigned protein chain.

Movie 2. Architecture of the *S. cerevisiae* NPC linker-scaffold.

An animated dissection of the composite structure generated by docking high-resolution crystal and single-particle cryo-EM structures into the S. cerevisiae ~25-Å NPC cryo-ET map (EMDB ID EMD-10198) (36). The nuclear envelope and protein cryo-ET densities are rendered as opaque and transparent gray isosurfaces, respectively. Crystal structures of nups and nup complexes are shown in cartoon representation. Unstructured linker connections between docked scaffolds are drawn as dashed lines.

Movie 3. Structural analysis of the NUP93^{SOL}•NUP53^{R2} structure.

Comparison of cartoon representations of *H. sapiens* NUP93^{SOL}•NUP53^{R2} with *S. cerevisiae* Nic96^{SOL} (PDB ID 2QX5) (59) and *C. thermophilum* Nic96^{SOL}•Nup53^{R2} (PDB ID 5HB3) (35) orthologs and comparison of conformational differences between apo NUP93^{SOL} and NUP93^{SOL}•NUP53^{R2} obtained from different crystal forms

Movie 4. Architecture of the symmetric core of the human NPC.

An animated dissection of the composite structure generated by quantitatively docking high-resolution crystal and single-particle cryo-EM structures into the human ~12-Å NPC cryo-ET map (EMDB ID EMD-14322) (47). The nuclear envelope and protein cryo-ET densities are rendered as opaque and transparent gray isosurfaces, respectively. Crystal structures of nups and nup complexes are shown in cartoon representation. Unstructured linker connections between docked scaffolds are drawn as dashed lines.

Movie 5. Dilation and constriction of the human NPC.

Interpolated transition between near-atomic composite structures of the symmetric core in the constricted state of the ~12-Å NPC cryo-ET map (EMDB ID EMD-14322) (47) obtained from purified nuclear envelopes and the symmetric core in the dilated state observed in the ~37-Å in situ cryo-ET map (EMDB ID EMD-11967) (45) of the human NPC. Enabled by linker-scaffold plasticity, the outward motion of the relatively rigid inner ring spokes enlarges the central transport channel and generates lateral channels between spokes.